AMERICAN
METEOROLOGICAL
SOCIETY

Journal of Climate

EARLY ONLINE RELEASE

This is a preliminary PDF of the author-produced manuscript that has been peer-reviewed and accepted for publication. Since it is being posted so soon after acceptance, it has not yet been copyedited, formatted, or processed by AMS Publications. This preliminary version of the manuscript may be downloaded, distributed, and cited, but please be aware that there will be visual differences and possibly some content differences between this version and the final published version.

The DOI for this manuscript is doi: 10.1175/JCLI-D-16-0424.1

The final published version of this manuscript will replace the preliminary version at the above DOI once it is available.

If you would like to cite this EOR in a separate work, please use the following full citation:

Murakami, H., G. Vecchi, T. Delworth, A. Wittenberg, S. Underwood, R. Gudgel, X. Yang, L. Jia, F. Zeng, K. Paffendorf, and W. Zhang, 2016: Dominant Role of Subtropical Pacific Warming in Extreme Eastern Pacific Hurricane Seasons: 2015 and the Future. J. Climate. doi:10.1175/JCLI-D-16-0424.1, in press.

© 2016 American Meteorological Society

Manuscript (non-LaTeX)
Click here to download Manuscript (non-LaTeX) draft_v20160906.docx

PRELIMINARY ACCEPTED VERSION

Dominant Role of Subtropical Pacific Warming in Extreme Eastern Pacific Hurricane Seasons: 2015 and the Future

Hiroyuki Murakami[1,2], Gabriel A. Vecchi[1,2], Thomas L. Delworth[1,2],

Andrew T. Wittenberg[1], Seth Underwood[3], Richard Gudgel[1], Xiaosong Yang[4],

Liwei Jia[1,2], Fanrong Zeng[1], Karen Paffendorf[1,2], and Wei Zhang[1,2]

[1]National Oceanic and Atmospheric Administration/Geophysical Fluid Dynamics Laboratory, Princeton, NJ, USA

[2]Atmospheric and Oceanic Sciences Program, Princeton University, Princeton, NJ, USA

[3]Engility, NOAA/GFDL, Princeton, NJ, USA

[4]University Corporation for Atmospheric Research, Boulder, CO, USA

Revised on 6 September 2016
Submitted to *Journal of Climate* on 1 June 2016

Corresponding author address: Hiroyuki Murakami, NOAA/GFDL, 201 Forrestal Rd., Princeton, NJ 08540-6649
E-mail: hir.murakami@gmail.com
Tel: 609-452-5824

Abstract

The 2015 hurricane season in the Eastern and Central Pacific Oceans (EPO and CPO), particularly around Hawaii, was extremely active – including a record number of tropical cyclones (TCs) and the first instance of three simultaneous Category 4 hurricanes in the EPO and CPO. A strong El Niño developed during the 2015 boreal summer season, and was attributed by some to be the cause of the extreme number of TCs. However, according to a suite of targeted high-resolution model experiments, the extreme 2015 EPO and CPO hurricane season was not primarily induced by the 2015 El Niño's tropical Pacific warming, but by warming in the subtropical Pacific Ocean. This warming is not typical of El Niño, but rather the "Pacific Meridional Mode (PMM)" superimposed on long-term anthropogenic warming. Although the likelihood of such an extreme year depends on the phase of natural variability, the coupled GCM projects an increase in the frequency of such extremely active TC years over the next few decades for the EPO, CPO, and Hawaii due enhanced subtropical Pacific warming from anthropogenic greenhouse forcing.

1. Introduction

The 2015 hurricane season in the Eastern Pacific Oceans (EPO; Northern Hemisphere 180–90ºW excluding the Atlantic Ocean) was extremely active. Twenty-seven tropical cyclones (TCs; maximum surface wind speed ≥34kt) were observed in the EPO in 2015 (Fig. 1a), the largest TC frequency since 1966 (Fig. 2a). The EPO can be divided into two subdomains: the Eastern EPO (EEPO; Northern Hemisphere 140–90ºW) and the Central Pacific Ocean (CPO; Northern Hemisphere 180–140ºW)[1]. Respectively, 18 and 9 TCs occurred in the EEPO and CPO in 2015 (Fig. 2b), the greatest TC frequency in the CPO since 1966 (the beginning of the satellite era, the point from which reliable TC frequency data in the eastern and central Pacific are available). This was the highest ratio TCs in the CPO relative to the EEPO (50%, red line in Fig. 2b), even though the TC frequency in the EEPO was also high (though not a record). Moreover, four TCs approached the shores of Hawaii (defined as the red shading in Fig. 1) during the 2015 hurricane season (orange bar in Fig. 2c), which is the 2nd largest number since 1966 (black bars in Fig. 2c). This season followed the active Central Pacific TC season of 2014, in which three TCs also approached Hawaii (Murakami et al. 2015a) – the first observed instance that three TCs approached the Hawaiian domain in two consecutive years.

Why was 2015 such an active in the EPO, CPO, and Hawaiian domain? Intrinsic ocean-atmosphere variability can result in strong variations in sea surface temperature (SST) and TC activity across the globe, including the EPO. In particular a strong El Niño developed during the 2015 boreal summer season (see red box in Fig. 3a), and a number of scientific and

Fig.1

Fig.2

Fig.3

[1] The National Hurricane Center and the Central Pacific Hurricane Center are in charge of monitoring/predicting TC activity in the EEPO and CPO, respectively, under the framework of the World Weather Watch (WWW) Programme of the World Meteorological Organization (WMO).

media reports attributed the extreme TC number to the strong El Niño event (e.g., The Weather Channel 2015; Thompson 2015; Liberto 2015). Indeed, previous studies reported substantial effect of El Niño on TC activity in the EPO and CPO (e.g., Chu and Wang 1997; Collins and Roache 2011; Jin et al. 2014; Kim et al. 2014; Vecchi et al. 2014; Murakami et al. 2015a; Krishnamurthy et al. 2016). During the summer of a developing El Niño the mean location of TC genesis shifts to the west, and TCs tend to track farther westward in the EPO (Chu 2004), resulting in a tendency for increase TC density in the CPO (e.g., Kim et al. 2014; Vecchi et al. 2014) – although there are indications that the response of EPO TCs to El Niño exhibits nonlinearities (e.g., Krishnamurthy et al. 2016). Jin et al. (2014) reported an increase in intense TCs in the following summer of an El Niño peak. Chu and Wang (1997) reported more TCs generate near Hawaii during El Niño developing years in the CPO. The correlation between TC frequency in the CPO and ENSO is 0.53 during 1966–1997 (Chu and Clark 1999). However, little is known about the factors responsible for the interannual variation of TC frequency in the EEPO as well as in the EPO. Whitney and Hobgood (1997) reported that there is no relationship between El Niño-Southern Oscillation (ENSO) and TC frequency in the EPO. Chu (2004) reported that the average annual number of TCs in the EPO is 15.1 (15.0) during El Niño (La Niña) years, indicating no difference between El Niño and La Niña years, based on the observed records from 1963 to 1993. Moreover, little is known about what controls extreme number of TC frequency in the EPO.

The Niño-3.4 SST anomaly (SSTA), a commonly used measure of the strength of El Niño, during May–November in 2015 was similar to that in 1997 (blue line in Fig. 2a and Fig. 3b). However, TC frequencies in the EPO, CPO, and the Hawaiian domain were close to normal in 1997, while the 2015 EPO TC season was extremely active (Fig. 1b and Fig. 2).

Why did more storms appear in 2015 than in 1997, despite similar central equatorial Pacific SSTA amplitude of the two El Niño events? In addition to El Niño, there are other modes of natural variability that may affect TC activity in the EPO and CPO. Murakami et al. (2015a) reported that the frequency of TCs approaching the Hawaiian domain has been found to be generally larger during the warm phases of ENSO (Chu and Wang 1997), Pacific Decadal Oscillation (PDO; Mantua 1997; Wang et al. 2010; Lupo et al. 2008), Interdecadal Pacific Oscillation (IPO; Power et al. 1999; Folland et al. 2002; England et al. 2014), and the cold phase of the Atlantic Multidecadal Oscillation (AMO; Delworth and Mann 2000). Kucharski et al. (2011) documented that the tropical Atlantic warming during the late 20th century might have led to a less Pacific warming through the Walker circulation. The reverse is true so that the cold phase of the AMO may lead more warming in the tropical EPO, which in turn leads to active TCs in the basin. Indeed, above climate indices are all favorable for TC activity in the EPO in the 2015 summer season (colored lines in Fig. 2a; see Supplementary Information for the definition of the climate indices). Therefore, based on historical relationships of climate indices to EPO TC activity alone, it is challenging to identify the cause of one active TC year.

In addition to the influence of internal variability on TC activity in the EPO and CPO, a number of previous studies reported projected increase in TC frequency in the CPO due to greenhouse-induced global warming (Li et al. 2010; Murakami et al. 2013; Knutson et al. 2015). The projected increase is principally associated with a north-westward shift of EPO TC tracks in the southeast of the Hawaiian islands, where climate models robustly predict greater warming than the rest of the tropics (Vecchi and Soden 2007; Murakami et al. 2013). Murakami et al. (2015a) investigated the influence of anthropogenic forcing and natural variability on the abnormal TC frequency near Hawaii in 2014, using a suite of climate

simulations. Murakami et al. (2015a) conclude that the extremely active 2014 Hawaiian hurricane season was made substantially more likely by anthropogenic forcing, but that natural variability (El Niño in particular) was also involved. In the present study, we build on methodology of Murakami et al. (2015a) to explore the factors responsible for the extremely active TC season for the EPO, CPO, and Hawaii in 2015. First we analyze observations and model simulations in order to understand effect of tropical (10°S–10°N, 170–80°W) and subtropical (10–35°N, 150–100°W) SST anomalies on TC frequency in the EPO. Also, we investigate possible future changes in the probability of occurrence of extremely active TC year like 2015 using a suite of climate simulations.

The remainder of this paper is organized as follows. Section 2 describes the models and data used in this study. Section 3a analyzes observations. Section 3b focuses on a possible cause of the extremely active 2015 TC year using idealized experiments under the framework of seasonal forecast. Section 3c,d investigates possible impact of anthropogenic warming and natural variability on frequency of occurrence for extremely active TC year. Finally, Section 4 provides conclusions and discussions of the results.

2. Methods

a. Observational datasets

In Section 3a, we first analyze observed TC frequency along with observed large-scale parameters in the EPO. The observed TC "best-track" data were obtained from the National Hurricane Center Best Track Database (HURDAT2; Landsea and Franklin 2013) as archived in the International Best Track Archive for Climate Stewardship (IBTrACS; Knapp et al. 2010) for the period 1966–2014. The data before 1966 are less reliable because satellite

observations were not sufficiently available for compiling TC data (Frank 1987). For the 2015 TC data, Unisys Corporation website (Unisys 2016) is used in this study. We also used the UK Met Office Hadley Centre SST product (HadISST1.1; Rayner et al. 2003) as observed SST for the period 1966–2015. For the precipitation data, Climate Prediction Center Merged Analysis of Precipitation (CMAP; Xie and Arkin 1997) was used for the period 1979–2015. For the atmospheric data, the Japanese 55-year Reanalysis (JRA-55; Kobayashi et al. 2015) for the period 1966–2015 was used. For the subsurface ocean temperature data, we used the GFDL ensemble couple data assimilation (ECDA; Zhang and Rosati 2010; Chang et al 2013) for the period 1966–2015.

To elucidate the potential influence of natural variability on the frequency of TCs in the EPO, we use above observations for computing indices of ENSO, Pacific Decadal Oscillation (PDO; Mantua et al. 1997), Interdecadal Pacific Oscillation (IPO; Power et al. 1999; Folland 2002; England et al. 2014), Pacific Meridional Mode (PMM; Chiang and Vimont 2004), and Atlantic Multidecadal Mode (AMO; Delworth and Mann 2000). The detailed calculation for the climate indices and spatial patterns are described in the Supplementary Information.

b. Models and TC detection method

We used the Geophysical Fluid Dynamics Laboratory (GFDL) Forecast-oriented Low Ocean Resolution model (FLOR; Vecchi et al. 2014). FLOR comprises approximately 50-km mesh atmosphere and land components, and approximately 100-km mesh sea ice and ocean components. Any simulations/forecasts by FLOR were conducted using “flux adjustment”, which adjusts the model’s air-sea fluxes of momentum, enthalpy, and freshwater to bring the

long-term climatology of SST and surface wind stress closer to the observations (Vecchi et al. 2014). Simulation characteristics, global climate sensitivity and forecast performance of FLOR are documented in a series of manuscripts (e.g., Vecchi et al. 2014; Winton et al. 2014; Msadek et al. 2014; Jia et al. 2015; Yang et al. 2015a; Delworth et al. 2015; Zhang and Delworth 2015; Krishnamurthy et al. 2015, 2016; Murakami et al. 2015b, 2016a,b; Zhang et al. 2016a,b). We also conducted idealized seasonal predictions using the atmospheric component of FLOR (i.e., AM2.5) by prescribing different SSTA spatial patterns in order to address relative importance of regional SSTA on the active 2015 TCs.

Model-generated TCs were detected directly from 6-hourly output, using the following tracking scheme developed in Harris et al. (2016), as implemented in Murakami et al. (2015b). In the detection scheme, the flood fill algorithm is applied to find closed contours of a specified negative sea level pressure (SLP) anomaly with a warm core. The TC detection must maintain warm core and wind criteria of 15.75 m s^{-1} for at least 36 consecutive hours. Because FLOR and AM2.5 has systematic model biases in basin-wide TC frequency, the simulated TC counts are calibrated using observed data: simulated TC counts are scaled by the ratio of the observed and predicted mean values for the period 1980–2015.

Throughout this study, we evaluate TC frequency and large-scale parameters during May–November because the official hurricane season defined by the U.S. National Weather Service extends from May to November (Chu 2004).

b. Retrospective seasonal forecasts

We first evaluate retrospective/real-time seasonal forecasts in order to evaluate if FLOR has skill in predicting active TCs in 2015 during the peak TC season (May–November)

as well as interannual variation of TC frequency. We conducted 12-member ensemble forecasts initialized on May 1st for each year in the period 1980–2015. The seasonal predictions were performed for 12-month duration for each ensemble member. The initial conditions for ocean and sea ice were derived from the coupled ensemble Kalman filter (EnKF; Zhang and Rosati 2010) data assimilation system developed for GFDL Coupled Model version 2.1 (CM2.1; Delworth el al. 2006; Gnanadesikan et al. 2006; Wittenberg 2006). However, the initial conditions for atmosphere and land components were not available because we do not have an assimilation system for them so far. Therefore, they were built through SST-forced atmosphere-land-only simulations using the atmospheric components of FLOR.

Figure 4 shows prediction skill for TC frequency for each ocean basins along with landfall frequency over the Hawaiian domain. FLOR could predict active TCs in 2015 in addition to the reasonable interannual variation of TC frequency. The correlation between predicted and observed TC frequency is significant for the EPO (r=0.63), EEPO (r=0.56), CPO (r=0.54), and the Hawaiian domain (r=0.53). Moreover, FLOR could predict extreme TC frequency in 2015 for all of the ocean basins. The reasonable forecast skill for other ocean basins (e.g., North Atlantic and western North Pacific) is also documented in Vecchi et al. (2014), Murakami et al. (2016a,b), and Zhang et al. (2016b). The high skill instills greater confidence for the use of the model to address the factors responsible for the active TC year of 2015. Meanwhile the observed TC count in 2015 for the CPO was out of range of the ensemble spread (Fig. 4c). It is not clear so far if the model deficiency is due to unpredictable stochastic processes in nature, or just because the model misses some processes related to the extreme TC frequency.

Fig.4

b. 1860/1990-control and multi-decadal simulations

In order to isolate effect of natural variability and anthropogenic forcing, we conducted control simulations and two types of 35-member ensemble multi-decadal simulations using FLOR. We first generated 3500-year control climate simulations (Murakami et al. 2015a; Yang et al. 2015b; Jia et al. 2016) using FLOR by prescribing radiative forcing and land-use conditions representative of the year 1860 (1860 Control). In addition, we generated 500-year control climate simulations by prescribing conditions representative of the year 1990 (1990 Control; Vecchi et al. 2014). These control experiments are free run in which reasonable internal variability of PDO (Zhang and Delworth 2015), ENSO (Vecchi et al. 2014; Krishnamurthy et al. 2016; Zhang et al. 2016a), and other internal variability of IPO and AMO are simulated given an arbitrary initial condition. The mean difference between the two control experiments is thought to be due to effect of anthropogenic forcing.

Two types of multi-decadal simulations were conducted for the period 1941 to 2040 (Fig. 5; Jia et al. 2016; Murakami et al. 2015a; Yang et al. 2015b). One of them is the all forcing experiment (AllForc), which uses prescribed Coupled Model Intercomparison Project Phase 5 (CMIP5) historical natural and anthropogenic forcing and aerosols up to 2005, and future projected levels based on the CMIP5 RCP4.5 scenario from 2006 to 2040. In the AllForc experiment, historical volcanic radiative forcing was also prescribed up to 2005; however, no volcanic forcing was prescribed after 2006. In an event of volcanic forcing, global mean surface temperature decreases (Fig. 5). Another simulation is the 1941 forcing experiment (1941Forc), which uses anthropogenic forcing (e.g., greenhouse gases, ozone, sulfate, etc.) fixed at the CMIP5 historical scenario 1941 level but time-varying CMIP5

Fig.5

natural forcings (e.g., solar forcing) from 1941–2040. Except for the differences in anthropogenic forcings, the 1941Forc and AllForc experiments use the same experimental settings (initial conditions, model settings, etc.). These multi-decadal simulations were not initialized to observed estimates of the climate state, but are initialized from a set of experiments that begin in 1861; *i.e.*, simulated internal variability generally was out of phase among the various ensemble members and observations (Murakami et al. 2015a; Yang et al. 2015b; Jia et al. 2016).

c. Empirical probability of exceedance

To estimate the potential probability of occurrence for the extreme TC-incidence years like 2015, we examine the empirical probability of exceedance for the frequency (Murakami et al. 2015a):

$$P(x) = \frac{Number\ of\ years\ with\ TC\ number \geq x}{Total\ number\ of\ years}$$

(1),

where x is the annual number of TCs. For example, $P(27)$ represents the probability of occurrence of a year with 27 or more TCs. For the 1860 (1990)-control experiments, we compute $P(x)$ using all 3500 (500) simulated years. To elucidate inter-centennial variability, we compute $P(x)$ for each 100-year period.

For the multi-decadal experiments, $P(x)$ was computed for each 20-year period from 1941 onward, yielding 700 (= 20 × 35) samples from which to calculate $P(x)$ (Fig. 5). Because the simulated internal variability is out of phase among the ensemble members, we can estimate for each 20-year period the conditional probability $P(x|Y_{\pm})$ under any phase of a natural mode of variability (i.e., Y_+ or Y_-). We define a positive (or negative) phase of ENSO,

PDO, IPO, PMM, and AMO when the May–November index amplitude exceeds one standard deviation (or falls below minus one standard deviation), and estimate the range of *P(x)* between the two phases.

d. Statistical Significance Test

To assess statistical significance for the simulated mean difference between 1860- and 1990-control experiments in terms of simulated TC frequency as well as TC density and large-scale parameters for each grid box, the bootstrap method proposed by Murakami et al. (2013) is applied. We avoid using the Student-t test to address statistical significance because TC frequency and TC density are not necessarily subject to a Gaussian distribution, but rather to a Poisson distribution. Therefore, a non-parametric method is preferable in these cases. First, the two datasets of 1860-control (3500 years) and 1990-control (500 years) experiments are combined (4000 years). Second, we perform 1000 resamplings of data, in which data were randomly picked from the combined data with replacement. The sampled data are assigned arbitrarily to the 1860-control or 1990-control group with the same sample size as the original data (i.e., 3500 and 500 years respectively); thereby, the sampling distribution is computed based on the difference between the resampled 1860-control and 1990-control groups. Finally, the P-value can be computed from the difference of the original data relative to the sampling distribution.

3. Results

a. Observed analysis for the extremely active 2015 TC year

As briefly mentioned in introduction, historical record of 27 (9) TCs are observed in the EPO (CPO) during 2015 summer season (Figs. 1,2). The mean TC frequency and one standard deviation are, respectively, 16.2 and 4.5 for the EPO, whereas those are 1.5 and 1.0 for the CPO. Therefore, anomaly of TC frequency in 2015 is +2.4σ for the EPO (and +7.5σ for the CPO), indicating extreme number of TC frequency in 2015. The Niño-3.4 index was also high (+2.36σ) in the 2015 summer season (Fig. 2a), resulting from extremely warm subsurface ocean conditions in the equatorial EPO in the 2015 summer season. This index was the 2nd highest since 1966, trailing slightly that of 1997 (=2.42σ). This observed co-occurrence might suggest that the odds of an extremely active 2015 TC season in the EPO and CPO were substantially enhanced by the development of this substantial El Niño event.

However, when we focus on the historical record of extremely active TC years in the EPO, they do not always emerge during an El Niño year (Figs. 2a and 6). We define extremely active TC years as those when the anomaly of TC frequency exceeds +1.0σ (which leads to the selection of 1982, 1984, 1985, 1990, 1992, 2014, and 2015). Among the seven extreme years, only two years (1982 and 2015; =29%) were during El Niño event (El Niño event is defined when the Niño-3.4 index exceeds +1.0σ; blue line in Fig. 2a). Meanwhile, there were two La Niña years (1984 and 1985) in the extreme TC years. Therefore, a full exploration of the historical record suggests a much more complex relationship between El Niño and extremely active TC years in the EPO, and it is likely that a big El Niño, like 2015, is not the only factor responsible for the emergence of extremely active TC years – even though some intense El Niño years are associated with extremely active EPO TC seasons (e.g., 1982 and 2015).

Fig.6

Generally, TC genesis in the EPO is most common in the latitudinal belt between 10° to 20°N (Fig. 6) whereas the Inter Tropical Convective Zone (ITCZ) is located to the south of

this latitudinal belt. We define the domain of most frequent TC genesis as the "Main Develop Region (MDR)". In the EEPO, MDR is defined as the blue box as shown in Fig. 6. This MDR was also defined in the previous study (Wu and Chu 2007). Although TC genesis is rare in the CPO, most of the TC genesis occurred in the red box in Fig. 6, and it is defined as the MDR for the CPO in this study. The 2015 summer season was characterized as weaker vertical wind shear in the both MDRs along with warmer central Pacific (Fig. 6a). Specifically vertical wind shear was historical low in the CPO MDR (Fig. 7c), and SSTA was historical high in the both EEPO and CPO MDRs (Figs. 7a,b). Moreover, mean mid-level relative humidity was historical high in the EEPO MDR (Fig. 7f), and mean low-level vorticity was also the highest over the CPO MDR (Fig. 7g). These results highlight that large-scale environment was extremely favorable for TC genesis during the 2015 summer seasons for both the EEPO and CPO MDRs.

Fig.7

In addition to the near-equatorial SSTA (*e.g.,* Niño-3.4), subtropical SSTA (10–35°N, 150–100°W) was also extremely high during the 2015 summer season (blue domain in Fig. 3a). To clarify the relative importance of the subtropical Pacific SSTA versus tropical Pacific SSTA, we can compare the TC activity of each season to the amplitude of tropical (10°S–10°N, 170–80°W) and subtropical (10°N–35°N, 150–100°W) SSTAs (Fig. 8a–c). The radius of a circle is proportional to TC frequency, and red color highlighting an extreme TC year defined as when the anomaly of TC frequency exceeds one standard deviation. For the EPO and EEPO (Figs. 8a,b), higher subtropical SSTA tends to show more frequent extreme TC years than the higher tropical SSTA does. Among the seven extreme TC years, four years show subtropical warming for the EPO (=57%, Fig. 8a) – a higher fraction than those co-occurring with tropical warming associated with El Niño (i.e., two out of seven extreme years;

Fig.8

=29%). However, there are exceptions, like 1984 and 1985, when both tropical and subtropical SSTAs were not large, indicating SSTA is not only the factor for the emergence of extreme TC years (or perhaps indicating the role of stochastic processes in seasonal TC activity). On the other hand, extreme years of the CPO TCs show a closer relationship with tropical SSTA in the observations than with subtropical SSTA (Fig. 8c), which is consistent with a previous study (Chu and Clark, 1999). Three out of seven extreme years (=43%) show extreme TC years in CPO during tropical warming years, whereas one out of seven extreme years (=14%) shows extreme TC years in CPO during subtropical warming years.

The positive SSTA over the subtropical EPO in 2015 is related to the positive phase of the Pacific Meridional Mode (PMM). The PMM is the internal coupled mode of ocean-atmosphere variability, involving coupling between winds, evaporation and ocean temperatures in the tropical and subtropical EPO (Chiang and Vimont 2004; see Supplemental Fig. S4). The positive PMM phase is characterized by a marked warming over the subtropical EPO and a cooling over the tropical EPO (Supplemental Fig. S4b). The subtropical SSTA related to the positive PMM generally peaks in the boreal spring (e.g., April–May), and it generally fades out during the boreal summer (e.g., July–September) in the EPO (Chiang and Vimont 2004). The PMM mode is also similar to the North Pacific Mode (NPM, Deser and Blackmon 1994), which is referred to the second mode of SST structures over the Pacific domain (20°S–60°N). Hartmann (2015) reported that positive NPM is characterized by a maximum positive SST anomaly centered round 45°N in the North Pacific along with the subtropical Pacific warming that is similar to the positive PMM pattern. Hartmann (2015) reported that the resent large positive NPM phase might have caused the severe winter in

North America in 2013–2014. The positive PMM is also thought to trigger some El Niño developing events (Chang et al. 2007; Zhang et al. 2009).

When we redraw Fig. 8a–c for the relationship between the Niño-3.4 and PMM indices (Fig. 8d–f), we obtain almost the same relationships as when the tropical and subtropical SSTs are used (Fig. 8a–c): Higher PMM index tends to show more extreme TC years in the EPO and EEPO than the Niño-3.4 index does. However, the large difference is apparent for 1997. Although the PMM index was positive during the 1997 boreal spring, it turned negative (–1.1σ) during the 1997 boreal summer, in spite of the slightly positive SSTA in the subtropics. On the other hand, the subtropical Pacific warming related to the positive PMM in 2015 remained throughout the summer time. We speculate that the difference in the subtropical warming may be one of the critical factors separating the active TCs in 2015 and normal TCs in 1997. To assess this hypothesis, we perform a series of idealized simulations in the next section.

Before moving to the model simulations, it is worthwhile comparing the impact of tropical SST warming and subtropical SST warming on the large-scale parameters in observations. For this purpose, we make two composites using observations. One of them is the composite of the large-scale parameters using the years with the subtropical SSTA more than +0.5σ but with the tropical SSTA less than +0.5σ (SUB; 1969, 1972, 1982, 1983, 1987, 1991, 2002, and 2006). Another are composites for those years with the tropical SSTA more than +0.5σ but with the subtropical SSTA less than +0.5σ (TRP; 1967, 1968, 1986, 1990, 1992, 1994, 1996, 2003, and 2004). Figure 9 shows composite of anomalies for SST, Fig.9 Precipitation, Ocean Thermal Energy Potential (OTEP, Gray 1975), mid-level relative humidity, vertical wind shear, and low-level relative vorticity for the SUB (left column) and

TRP (right column). Note that the composite for precipitation were made from 1979 because the CMAP data is available from 1979. OTEP (units=cal cm^{-2}) is a measure of warmness of subsurface ocean defined as follows.

$$OTEP = \int_{surface}^{60m\ or\ where\ T=26°C} \rho_w c_w (T - 26) dz$$

(2),

where T is ocean temperature (°C), ρ_w is ocean density (1 gm cm^{-3}), c_w is the specific heat of water (1 cal gm^{-1} °C). A large OTEP value is favorable for TC development through abundant thermal energy without losing energy by the storm-induced cold wake (Gray 1975).

Overall, all of the variables show more favorable conditions for TC genesis in the SUB composites relative to the TRP composites over the MDRs: larger precipitation (Figs. 9c,d), higher OTEP (Figs. 9e,f), higher relative humidity (Figs. 9g,h), weaker vertical wind shear (Figs. 9i,j), and larger positive vorticity (Figs. 9k,l). The composite results for the vertical wind shear is consistent with the previous study of Larson et al. (2012). Therefore, the subtropical warming brings more favorable large-scale conditions for TC genesis rather than the tropical Pacific warming does. Specifically, the composite for precipitation (Figs. 9c,d) suggests that the ITCZ shifts poleward during the subtropical warming years relative to the climatological mean, whereas the ITCZ slightly shifts equatorward during the tropical warming years. Although it is in the model world, Merlis et al. (2013) reported that simulated location of the ITCZ is critical for simulated TC frequency: an increase in TC frequency as the ITCZ shifts poleward. Although sample size is limited for observations, the 500-yr 1990-control simulation with more samples shows consistent results (figure not shown).

In the next section, we further investigate relative importance of the subtropical Pacific and tropical SSAs, in addition to the SSTAs in other ocean basins, to the extreme TC year of 2015 under the framework of seasonal forecast.

b. Idealized retrospective seasonal forecast

As mentioned in the previous section, the spatial pattern and magnitudes of SSTAs in the 2015 summer season resembles those observed in 1997 (Figs. 3a,b): marked warming in the tropical and subtropical EPO; Indian Ocean; and slight cooling in the tropical North Atlantic. To assess the relative importance of the above regional SSTAs to the active TCs in 2015, we conduct idealized 12-member ensemble predictions using the atmosphere component of FLOR (i.e., AM2.5) initialized on 1st May 2015, and driven by various prescribed SSTA patterns. The three control experiments are so-called "CLIMSST", "ANOM1997", and "ANOM2015" in which SSTAs are set to zero, 1997 observed values (shading in Fig. 3b), or 2015 FLOR predicted values (shading in Fig. 3a), respectively. Figure 10 show the predicted TC frequency in the EPO, EEPO, CPO, and near Hawaii, respectively. The ANOM2015 shows markedly more TCs than the CLIMSST and ANOM1997 experiments, consistent with the observations and FLOR predictions (Figs. 1,2, and 4). The experiments ATLCLIM and INDCLIM resemble the ANOM2015, except that SSTAs are set to zero over the Atlantic Ocean and Indian Ocean, respectively (Figs. 3e,f). These experiments show only small differences from the ANOM2015 in terms of simulated TC frequency, indicating that the SSTAs in these basins do not strongly influence the 2015 TC activity in the model predictions. The ATLCLIM slightly shows decreases in TC frequency from the ANOM2015 for all of the domains, especially in the CPO, indicating that the cooler Atlantic Ocean influenced the TC

Fig.10

activity in the domains through the teleconnection as reported by Kucharski et al. (2011) and Wang and Lee (2009). The SPCLIM is the same as the ANOM2015, except that SSTAs are set to zero north of 15°N in the EPO (Fig. 3c). Conversely, in the SPANOM experiment the SSTA is set to zero everywhere *except* north of 10°N in the EPO, where the 2015 SSTA is prescribed (Fig. 3d). These idealized experiments show increased TC frequency in response to positive SSTAs over the subtropical EPO.

Note that even though the tropical warm SSTA associated with El Niño is removed in the SPANOM, this experiment shows the highest number of storms among the idealized experiments except for the CPO. This suggests that the 2015 active TC season is more likely attributable to the warm conditions in the subtropical EPO, than those in the tropical EPO. That SPCLIM has even fewer storms than the CLIMSST does except for the CPO further suggests that taken in isolation, the tropical component of the El Niño SSTAs actually suppress TC activity in most of the subdomains. It is possible that some of the SPANOM SSTAs were themselves related to El Niño; indeed they were also evident, to lesser extent, in 1997 (Fig. 3b).

c. Influence of anthropogenic forcing on occurrence of active TC year like 2015

Previous section highlights that the subtropical surface warming is a key for the extreme TC year in 2015. On the other hand, a number of state-of-the-art climate models consistently project more warming in the subtropical Pacific relative to the other open oceans (e.g, Xie et al. 2010; Murakami et al. 2013). Therefore, it is possible that anthropogenic forcing might have partially contributed to the extremely warm subsurface ocean in the subtropical Pacific, and that in turn leads to the extreme TC year in 2015. In order to elucidate

influence of anthropogenic forcing on the probability of occurrence of the extreme TC year like 2015, we analyzed results from long control runs with forcing fixed at either 1860 conditions (3500-year simulation) or 1990 conditions (500-year simulation).

The mean SST difference between these two control experiments is shown in Fig. 11a, revealing relatively higher SST for 1990 conditions in the subtropical EPO – this enhanced subtropical Pacific warming consistently emerges in studies of the response of SSTs to increasing greenhouse gases (Xie et al. 2010; Murakami et al. 2013). Figure 11b shows projected changes in TC genesis density. TC genesis positions are counted for each 2.5° × 2.5° grid box within the global domain. The total count for each grid box is defined as the TC genesis density. It is noted that TC genesis shifts toward center of Pacific, which is consistent with the previous studies (Li et al. 2010; Murakami et al .2013). Over the MDRs in the EPO (blue) and CPO (red), TC genesis is more frequent in the 1990 control experiments than in the 1860 experiment. Table 1 shows mean difference in TC frequency between the 1990- and 1860-control experiments for each domain in the EPO. It shows statistically significant increases in the mean TC frequency for all of the domains.

Fig.11

Projected increase in frequency of occurrence of extremely active TC year is also expected from the projected increase in TC genesis frequency. Following Murakami et al. (2015a), we will examine the empirical probability of exceedance for the frequency of TCs as a function of TC number [i.e., *P(x)*; See Section 2c] in response to anthropogenic radiative forcing changes. Figure 12 shows that the probability of occurrence for an extreme event in the 1990-control than in the 1860-control experiment. Here, extreme range of x is taken from the value of $+1\sigma$ for the anomaly of TC frequency based on the 1966–2015 observations (i.e., EPO=21, EEPO=19, CPO=3, and Hawaii=1). Overall, the probability increases significantly

Fig.12

from the 1860-control to the 1990 control for all the domains. The fraction of attributable risk (FAR; Jaeger et al. 2008) is computed for the estimation of the impact of anthropogenic forcing. FAR is defined as follows:

$$FAR(x) = \frac{P(x|E_1) - P(x|E_0)}{P(x|E_1)}$$

(3),

where E_1 is anthropogenic warming condition, whereas E_0 natural forcing alone. FAR ranges from $-\infty$ (not attributable) to 100% (attributable). In the control experiments, FAR ranges from 60–80% for the EPO, 40–60% for the EEPO, 70–100% for the CPO, and 70–100% for the Hawaiian domain (green marks in Fig. 12), suggesting that anthropogenic forcing substantially changes the odds of extreme TC seasons like 2015 relative to natural variability alone.

d. Influence of internal variability and anthropogenic forcing on occurrence of extreme TC year like 2015

Generally, more TCs are observed during the positive phase of ENSO (blue), PMM (red), IPO (purple), and PDO (green), and negative phase of AMO (yellow) in the EPO (Fig. 2a). To discriminate the potential influence of natural variability versus anthropogenic forcing on extreme event of TC activity, we analyzed the two 35-member ensembles of simulations, run from 1941 to 2040. In the first ensemble, called “AllForc”, the simulations were driven by estimates of observed changes in anthropogenic radiative forcing from greenhouse gases and aerosols, as well as projections of future changes based on the representative concentration pathway (RCP) 4.5 scenario. In the second ensemble, called “1941Forc”, the simulations used

constant greenhouse gas and aerosol forcing representative of 1941 conditions. The difference in the mean of the ensembles between the AllForc and 1941Forc is mainly due to the effect of anthropogenic forcing. In addition, responses of the anthropogenic forcing can be estimated by taking mean of the 35 members for the AllForc experiment because the model generated internal variability within each ensemble member is canceled out by the mean operation.

Figure 13 shows the difference in projected mean SST and TC genesis density between the AllForc and 1941Forc experiments for each 20-year period from 1941. The simulated difference in SST between the AllForc and 1941Forc experiments gradually becomes larger as time proceeds with more warming in the subtropical central Pacific (Fig. 13a–e), which is consistent with the control experiments (Fig. 11a). Impacts of warming on TC genesis density and basin-total TC genesis frequency are generally consistent with those in the control experiments (Fig. 13f–j and Table 2): increases of TC genesis frequency in the both EEPO and CPO. A detailed difference from the control experiments is the larger tropical SST anomaly (10°S–10°N) during period 2021–2041 that is equivalent to the warming in the subtropical Pacific (Fig. 13e). Another difference is that the decrease in TC genesis density along the coastline of Mexico is larger than that in the control experiments (Figs. 11b, 13j). Consequently, projected changes in basin-total TC genesis frequency in the EEPO for 2001–2020 and 2021–2041 are smaller than that in the control experiments, although they are still positive change (Table 2). Fig.13

Figure 14 summarizes the role of radiative forcing and natural large-scale ocean patterns in altering the probability of occurrence of a hyper-active TC season like that of 2015. Note that because the control experiments did not record 9 TCs in the CPO (Fig. 12c), probability of the occurrence of the year with 8 or more TCs is evaluated for the CPO instead. Fig.14

Orange marks in Fig. 14 reveal *P(x)* for the fixed forcing control simulations (see Section 3c), showing again that the probability of occurrence for an extreme event like that predicted for 2015 is higher in the 1990-control than in the 1860-control experiment. This increased TC incidence is also consistent with the multi-decadal simulations, as can be seen by comparing the AllForc (black lines) to the 1941Forc (gray lines) in Fig. 14, although the difference in *P(19)* for the EEPO is not much clear between the AllForc and 1941Forc, especially after 2000 (Fig. 14b). Therefore, influence of anthropogenic forcing on the increase in *P(x)* is larger in the CPO than in the EEPO. It is interesting that these results are consistent with the 2015 TC season: extreme TC frequency in the CPO and moderately active TCs in the EEPO. Overall, the simulations suggest that even subject to a rare confluence of forcings from several natural climate modes, anthropogenic climate change would still have boosted the odds of an extremely active 2015 TC season in the EPO.

The color bars in Fig. 14 reveal the effect of natural variability on the probability of occurrence in the AllForc ensemble members. The relatively wide bars in Fig. 14 highlight the marked influence of natural variability on the probability. In general, for TC incidence in each region, the influences of the PDO and IPO are smaller than those of the PMM and ENSO. On the other hand, the AMO excites larger variability of *P(x)* than the PDO and IPO do. It appears that the PMM has the largest influence on the variability of *P(x)* in the model experiments. The extremely large number of TCs during the 2015 hurricane season occurred under favorable PMM (+0.9), El Niño (+2.3), and AMO (–1.7). Moreover, defining *E* as the event in which the PMM and ENSO indices are all positive and AMO index is negative, as in 2015 (Figs. 2a), we find from the 1990 control that *P(x|E)* is about 2.6 (FAR=61%), 1.3 (FAR=22%), 6.0 (FAR=83%), and 7.0 (FAR=86%) times higher than those from the 1860

control experiment for *P(27)* of the EPO TCs, *P(19)* of the EEPO TCs, *P(8)* of the CPO TCs, and *P(4)* of the Hawaiian TCs, respectively. Therefore, it is possible that global warming increased the odds of the extremely large number of the EPO and CPO TCs in 2015 even during the similar conditions of natural variability.

Above discussions do not give any answers for which of positive PMM and El Niño strictly plays an important role for triggering the extremely active TC year of 2015, because positive PMM sometimes coincides with El Niño. Moreover, Fig. 14 shows that a negative AMO phase provides considerable impact on the variation of *P(x)*, especially for the CPO. However, again, some of the negative AMO years coincide with positive PMM and ENSO years. Therefore, we further computed conditional *P(x)*, namely, *P(x|E)* under the five conditions of E1–E5 in order to strictly separate the effect of the single natural variability from others. The E1 is the combined condition when PMM $\geq +1\sigma$, Niño-3.4 $\geq +1\sigma$, and AMO $\leq -1\sigma$, implying similar condition to the 2015 summer season. The E2 is for the years with PMM $\geq +1\sigma$, but Niño-3.4 $< +1\sigma$ and AMO $> -1\sigma$, as an indication of PMM only effect by excluding the El Niño and negative AMO. The E3 is for the years when Niño-3.4 $\geq +1\sigma$, but PMM $< +1\sigma$ and AMO $> -1\sigma$, namely, El Niño only effect. The E4 is for the years when AMO $\leq -1\sigma$, but PMM $< +1\sigma$ and Niño-3.4 $< +1\sigma$, as an indication of AMO only effect. The E5 is for the years with PMM $< +1\sigma$, Niño-3.4 $< +1\sigma$, and AMO $> -1\sigma$, representing no effect. Figure 15 shows the conditional probability of exceedance using the AllForc experiment for 2001–2020 period in which 2015 is included. Figure 15 highlights that the *P(x|E1)* is the highest for most of the basins and most of the TC numbers, as expected. Moreover, *P(x|E2)* is much larger than *P(x|E3)* and *P(x|E4)*, in addition to that *P(x|E2)* is closer to *P(x|E1)*. This indicates that the odds of occurrence of the extreme TC event in the EPO, EEPO, CPO, and the Hawaiian

Fig.15

domain increase a lot by the positive PMM only. FAR is computed from the basis of E5 (i.e., E_0 = E5 in Eq. 3) in Fig. 15. FAR is about 60–80% for E2 in the EPO (blue circles), whereas that is about 20–40% for E3 (green circles) and 0% or negative for E4 (pink circles) in the EPO. And above results are generally and qualitatively consistent for the EEPO (Fig. 15b), CPO (Fig. 15c), and the Hawaiian domain (Fig. 15d). Therefore, the 2015 extreme TC events may be due mostly to the positive PMM, namely, the subtropical Pacific warming, rather than the tropical Pacific warming by the big El Niño and the tropical Atlantic cooling by the negative AMO phase. Because FAR is still about 20–40% for E3 for the EPO (Fig. 15a), we cannot completely rule out the effect of the big El Niño on the emergence of the extremely active TCs in 2015. However, from the above discussions, it is likely that the positive PMM gave a larger impact on the active TCs in the EPO than the big El Niño did.

4. Conclusions and discussions

The 2015 hurricane season in the EPO and CPO, particularly around Hawaii, was extremely active. There were historical record of 27 (9) TCs observed in the EPO (CPO). In addition, three hurricanes approached Hawaiian Islands in the year. The Niño-3.4 index was also high in the 2015 summer season. The observed co-occurrence of active TCs and the strong El Niño in the EPO brought scientific arguments if the active 2015 TC year arose by the strong El Niño development.

However, the observed record since 1966 shows that the extremely active TC years in the EPO do not always arise during the tropical Pacific warming years (i.e., El Niño years). Meanwhile, they arise more frequent during the subtropical Pacific warming years than the tropical Pacific warming years. Moreover, reanalysis data show that the large-scale conditions

are more favorable for TC genesis over the MDRs for the EEPO and CPO during the subtropical Pacific warming years than the tropical Pacific warming years. The positive SSTA over the subtropical EPO in 2015 is mainly associated with the positive phase of PMM with some possible contributions from the decadal variation of PDO, IPO, and AMO. Moreover, the state-of-the-art climate models commonly project substantial subtropical Pacific warming in the future by anthropogenic forcing. Therefore, we hypothesize that the active 2015 TCs in the EPO was mostly caused by the subtropical Pacific warming mostly associated with the internal variability of positive PMM phase, superimposed on the anthropogenic global warming effect, rather than the tropical Pacific warming associated with El Niño development.

To support the hypothesis, the suite of fixed forcing control simulations, seasonal predictions, and multi-decadal simulations were conducted using FLOR/AM2.5. These results suggest that the extreme TC frequency in 2015 was mainly linked to a positive PMM, with a weaker link to El Niño. Furthermore, the model experiments indicate that the impact of the PMM on the EPO, EEPO, CPO and the Hawaiian TCs in 2015 occurred in the context of an underlying increase in the probability of years with extreme TC activity due to anthropogenic forcing. The projected probability of exceedance continues to increase through 2020–2040 in the EPO due to anthropogenic forcing, especially for the CPO and the Hawaiian domain – arising in large part due to projections for an enhanced surface warming in the subtropical Pacific in response to increasing greenhouse gases (Vecchi and Soden 2007; Xie et al. 2010; Li et al. 2010; Murakami et al. 2013). Moreover, The decadal natural variability of the IPO and PDO might have also changed the sign recently (Fig. 2), leading to more favorable conditions for the occurrence of an extremely active TC year in the EPO. Klotzbach et al. (2015) also reported that the AMO might have switched phase to negative in 2014 or 2015

(Supplementary Fig. S5). Therefore, it is possible that the change in AMO phase might have caused the active 2015 TC year. However, further analysis for the multi-decadal simulations showed that the negative AMO alone did not influence the increase of probability of occurrence of the active TC season like 2015 for all of the ocean basins. It is rather positive PMM alone that caused the increase of the probability of extreme TC season than El Niño and negative AMM. These results indicate that extreme years, like 2015, are likely to become more common in the near future, although subject to strong intrinsic modulation arising mainly from the PMM.

We stress that our finding is a model-based attribution, and does not constitute a detectable anthropogenic influence at this stage. In particular, the relatively-short (~50 year) time series of the observed TC frequency in the EPO, EEPO, CPO, and near Hawaii do not show a rising trend over time (Fig. 2). This lack of detection may be due to the pronounced internal climate variability of TC occurrence in these regions, or it could indicate a deficiency in the modeled sensitivity of TCs in the EPO, EEPO, CPO, and Hawaii. Assessment of model-based attribution, and related projection, would benefit immensely from a longer relatively-homogeneous record of the EPO, EEPO, CPO and Hawaiian TCs, as presently exists for the Atlantic (Landsea et al. 2004; Landsea et al. 2010).

Acknowledgments The authors thank Dr. Shukuro Manabe, Dr. Thomas R. Knutson, and Dr. Nathaniel Johnson for their suggestions and comments. This report was prepared by HM under award NA14OAR4830101 from the National Oceanic and Atmospheric Administration, U.S. Department of Commerce. The statements, findings, conclusions, and recommendations are those of the authors and do not necessarily reflect the views of the National Oceanic and

Atmospheric Administration, or the U.S. Department of Commerce.

References

Chang, P., Li. Zhang, R. Saravanan, D. J. Vimont, J. C. H. Chiang, L. Ji, H. Seidel, and M. K. Tippet, 2007: Pacific meridional mode and El Niño–Southern Oscillation, *Geophys. Res. Lett.* **34,** L16608.

Chang, Y. -S., S. Zhang, A. Rosati, T. L. Delworth, and W. F. Stern, 2013: An assessment of oceanic variability for 1960–2010 from the GFDL ensemble coupled data assimilation. Climate Dynamics, doi:10.1007/s00382-012-1412-2.

Chiang, J. C. H., and D. J. Vimont, 2004: Analogous Pacific and Atlantic meridional modes of tropical atmosphere–Ocean variability *J. Climate*, **17,** 4143–4158.

Chu, P.-S., and J. D. Clark, 1999: Decadal variations of tropical cyclone activity over the central North Pacific. *Bull. Amer. Meteor. Soc.*, **80,** 1875–1881.

Chu, P.-S., and J. Wang., 1997: Tropical cyclone occurrences in the vicinity of Hawaii: Are the difference between El Niño and Non-El Niño years significant? *J. Climate*, **10,** 2683–2689.

Chu, P.-S., 2004: ENSO and tropical cyclone activity. Hurricanes and Typhoons: Past, Present, and Potential. R. J. Murnane and K.-B. Liu, Eds., Columbia University Press, 297-332.

Collins, J.M. and D. R. Roache, 2011: The hurricane season in the Eastern North Pacific Basin: An analysis of environmental conditions. *Mon. Wea. Rev.,* **139(6),** 1673–1682.

Delworth, T. L., and M. E. Mann, 2000: Observed and simulated multidecadal variability in the Northern Hemisphere. *Climate Dyn.* **16,** 661–676.

Delworth, T. L., and co-authors, 2006: GFDL's CM2 global coupled climate models. Part I: Formulation and simulation characteristics. *J. Climate*, **19,** 643–674.

Delworth, T.L., and co-authors, 2015: A link between the hiatus in global warming and North American drought. *J. Climate*, **28,** 3834–3845, doi: 10.1175/JCLI-D-14-00616.1

Deser, C., and M. L. Blackmon, 1995: On the relationship between tropical and North Pacific sea-surface temperature variations. *J. Climate*, **8(6),** 1677–1680,

England, M. H., and coauthors, 2014: Recent intensification of wind-driven circulation in the Pacific and the ongoing warming hiatus. *Nat. Climate Change*, **9,** 222–227.

Frank, W. M., 1987: Tropical cyclone formation. *A Global View of Tropical Cyclones*, R. L. Elsberry, W. M. Frank, G. J. Holland, J. D. Jarrell, and R. L. Southern, Eds., Naval Postgraduate School, 53–90.

Folland, C. K., J. A. Renwick, M. J. Salinger, and A. B. Mullan, 2002: Relative influences of the Interdecadal Pacific Oscillation and ENSO on the South Pacific Convergence Zone. *Geophys. Res. Lett.* **29,** 211–214.

Gnanadesikan, A., and co-authors, 2006: GFDL's CM2 global coupled climate models. Part II: The baseline ocean simulation. *J. Climate*, **19,** 675–697.

Gray, W. M., 1975: Tropical cyclone genesis, Dept. of Atmospheric Science Paper No. 234, Colorado State University, Fort Collins, CO, 121 pp.

Hartmann, D. L., 2015: Pacific sea surface temperature and the winter of 2014. *Geophys. Res. Lett.* **42,** doi: 10.1002/2015GL063083.

Harris, L.M, S.-J. Lin, and C.Y. Tu, 2016: High resolution climate simulations using GFDL HiRAM with a stretched global grid. *J. Climate*, **29,** 4293–4314.

Jaeger, C.C., J. Krause, A. Haas, R. Klein, and K. Hasselmann, 2008: A method for computing the fraction of attributable risk related to climate damages. *Risk Analysis,* **28,** 815–823.

Jia, L. and coauthors (2015): Improved Seasonal Prediction Skill of Land Temperature and Precipitation in a GFDL High-Resolution Climate Model, *J. Climate*, **28,** 2044–2062, doi:10.1175/JCLI-D-14-00112.1

Jia, L.; G.A. Vecchi; X. Yang; R. Gudgel; T. Delworth; W. Stern; K. Paffendorf; S. Underwood; F. Zeng, 2016: The Roles of Radiative Forcing, Sea Surface Temperatures, and Atmospheric and Land Initial Conditions in U.S. Summer Warming Episodes. *J. Climate*, **29,** 4121–4135.

Jin, F.-F., J. Boucharel, and I.-I. Lin., 2014: Eastern Pacific tropical cyclone intensified by El Niño delivery of subsurface ocean heat. *Nature,* **516,** 82–85.

Kim, H.-S., and co-authors, 2014: Tropical cyclone simulation and response to CO_2 doubling in the GFDL CM2.5 high-resolution coupled climate model. *J. Climate*, **27,** 8034–8054.

Klotzbach, P., W. Gray, and C. Fogarty, 2015: Active Atlantic hurricane era at its end? *Nature Geoscience,* **8,** 737–738.

Knapp, K. R., M. C. Kruk, D. H. Levinson, H. J. Diamond, and C. J. Neuman, 2010: The international best track archive for climate stewardship (IBTrACS): Unifying tropical cyclone best track data, *Bull. Amer. Meteor. Soc.*, **91**, 363–376.

Knutson, T. R., and coauthors., 2015: Global projections of intense tropical cyclone activity for the late twenty-first century from dynamical downscaling of CMIP5/RCP4.5 scenarios. *J. Climate*, **28,** 7203–7224.

Kobayashi, S., and co-authors, 2015: The JRA-55 reanalysis: General specifications and basic characteristics. *J. Meteor. Soc. Japan*, **93**, 5–48.

Krishnamurthy, L., G. Vecchi; R. Msadek; A. Wittenberg; T. Delworth; F. Zeng, 2015: The Seasonality of the Great Plains Low-Level Jet and ENSO Relationship. *J. Climate*. doi:10.1175/JCLI-D-14-00590.1

Krishnamurthy, L., G. A. Vecchi, R. Msadek, H. Murakami, A. Wittenberg, and F. Zeng, 2016: Impact of strong ENSO on regional tropical cyclone activity in a high-resolution climate model. *J. Climate*, **29**, 2375–2394.

Kucharski, K., I.-S. Kang, R. Farneti, and L. Feudale, 2011: Tropical Pacific response to 20th century Atlantic warming., *Geophys. Res. Lett.* **38,** L03702.

Landsea, C. W., and coauthors, 2004: The Atlantic hurricane database reanalysis project: Documentation for the 1851–1910 alterations and additions to the HURDAT database. *Hurricanes and Typhoons: Past, Present and Future*, R. J. Murname and K.-B. Liu, Eds., Columbia University Press, 177–221.

Landsea, C. W., G. A. Vecchi, L. Bengtsson, and T. R. Knutson, 2010: Impact of duration thresholds on Atlantic tropical cyclone counts. *J. Climate*, **23,** 2508–2519.

Landsea, C. W., and J. L. Franklin, 2013: Atlantic hurricane database uncertainty and presentation of a new database format. *Mon. Wea. Rev.*, **141,** 3576–3592.

Larson, S.M., S.-K. Lee, C. Wang, E.-S. Chung, and D. Enfield, 2012: Impacts of non-canonical El Niño patterns on Atlantic hurricane activity. *Geophys. Res. Lett.,* **39,** L14706.

Li, T., M. Kwon, M. Zhao, J.-S. Kug, J.-J Luo, and W. Yu., 2010: Global warming shifts Pacific tropical cyclone location. *Geophys. Res. Lett.,* **37,** L21804.

Liberto, T. D., 2015: Central Pacific hurricane party: three's company. [Available online at https://www.climate.gov/news-features/event-tracker/central-pacific-hurricane-party-three's-company]

Lupo, A. R., T.K. Latham, T. Magill, J. V. Clark, C. J. Melick, and P.S. Market, 2008: The interannual variability of hurricane activity in the Atlantic and East Pacific regions. *Nat. Wea.* Dig., **32(2),** 119–135.

Mantua, N. J., S.R. Hare, Y. Zhang, J. M. Wallace, and R. C. Francis, 1997: A Pacific interdecadal climate oscillation with impacts on salmon production. *Bull. Amer. Meteor. Soc.,* **78,** 1069–1079.

Merlis, T. M., M. Zhao, and I. M. Held, 2013: The sensitivity of hurricane frequency to ITCZ changes and radiatively forced warming in aquaplanet simulations. *Geophys. Res. Lett.,* **40,** 4109–4114.

Msadek, R., G.A. Vecchi, M. Winton, R.G. Gudgel, 2014: Importance of initial conditions in seasonal predictions of Arctic sea ice extent. *Geophys. Res. Lett.,* **41**, 5208–5215, doi:10.1002/2014GL060799

Murakami, H., B. Wang, T. Li, and A. Kitoh., 2013: Projected increase in tropical cyclones near Hawaii. *Nat. Climate Change*, **3,** 749–754.

Murakami, H., G. A. Vecchi, T. L. Delworth, K. Paffendorf, R. Gudgel, L. Jia, and F. Zeng, 2015a: Investigating the influence of anthropogenic forcing and natural variability on the 2014 Hawaiian hurricane season. [in "Explaining Extremes of 2014 from a Climate Perspective"]. *Bull. Amer. Meteor. Soc.*, S115–S119.

Murakami, H., G. A. Vecchi, S. Underwood, T. L. Delworth, A. T. Wittenberg, W. G. Anderson, J. -H. Chen, R. G. Gudgel, L. Harris, S. -J. Lin, and F. Zeng, 2015b: Simulation and prediction of Category 4 and 5 hurricanes in the high-resolution GFDL HiFLOR coupled climate model. *J. Climate*, **28**, 9058-9079.

Murakami, H., G. Villarini, G. A. Vecchi, W. Zhang, and R. Gudgel, 2016a: Statistical-dynamical seasonal forecast of North Atlantic and U.S. landfalling tropical cyclones using the high-resolution GFDL FLOR coupled model. *Mon. Wea. Rev.*, **144**, 2101-2123.

Murakami, H., G. A. Vecchi, G. Villarini, T. L. Delworth, R. Gudgel, S. Underwood, X. Yang, W. Zhang, and S. Lin, 2016b: Seasonal forecasts of major hurricanes and landfalling tropical cyclones using a high-resolution GFDL coupled climate model. *J. Climate*, in press.

Power, S., T., Casey, C. Folland, A. Colman, and V. Mehta, 1999: Interdecadal modulation of the impact of ENSO on Australia. *Climate Dyn.* **15,** 319–324.

Rayner, N. A., D. E. Parker, E. B. Horton, C. K. Folland, L. V. Alexander, and D. P. Rowell, 2003: Global analysis of sea surface temperature, sea ice, and night marine air temperature since the late nineteenth century. *J. Geophys. Res*., **108**, 4407.

The Weather Channel, 2015: Three Category 4 Hurricanes in the Pacific Ocean: How Rare Is That? [Available online at http://www.weather.com/storms/hurricane/news/three-category-4-hurricanes-pacific-kilo-ignacio-jimena]

Thompson, A., 2015: El Niño Helps Boost Pacific Storm Season. [Available online at http://www.climatecentral.org/news/el-nino-boosts-pacific-storms-19210]

Unisys, 2016: Unisys weather hurricane tropical data. [available online at http://weather.unisys.com/hurricane/]

Vecchi, G.A. and B.J. Soden, 2007: Effect of remote sea surface temperature change on tropical cyclone potential intensity. *Nature*, **450**, 1066-1070 doi:10.1038/nature06423.

Vecchi, G. A., and co-authors, 2014: On the seasonal forecasting of regional tropical cyclone activity. *J. Climate*, **27,** 7994–8016.

Wang, B., Y. Yang, Q.-H. Ding, H. Murakami, and F. Huang, 2010: Climate control of the global tropical storm days (1965-2008). *Geophys. Res. Lett.,* **37,** L07704.

Wang, C., and S.-K. Lee, 2009: Co-variability of tropical cyclones in the North Atlantic and the eastern North Pacific.). *Geophys. Res. Lett.,* **36,** L24702.

Whitney, L. D., and J. Hobgood, 1997: The relationship between sea surface temperatures and maximum intensities of tropical cyclones in the eastern North Pacific Ocean. *Climate*, **10,** 2921–2930.

Winton, M., W.G. Anderson, T.L. Delworth, S.M. Griffies, W.J. Hurlin, and A. Rosati, 2014: Has Coarse Ocean Resolution Biased Simulations of Transient Climate Sensitivity? *Geophys. Res. Lett.*, **41**(23), DOI:10.1002/2014GL061523

Wittenberg, A. T., A. Rosati, N. –C. Lau, and J. J. Ploshay, 2006: GFDL's CM2 global coupled climate models. Part III: Tropical pacific climate and ENSO. *J. Climate*, **19,** 698–722.

Wu, P., and P.-S. Chu, 2007: Characteristics of tropical cyclone activity over the eastern North Pacific: the extremely active 1992 and the inactive 1997. *Tellus*, **59A,** 444–454.

Xie, P., and P. A. Arkin, 1997: Global precipitation: A 17-year monthly analysis based on gauge observations, satellite estimates, and numerical model outputs. *Bull. Amer. Meteor. Soc.,* **78,** 2539–2558.

Xie, S.-P., C. Deser, G. A. Vecchi, J. Ma, H. Teng, and A. T. Wittenberg, 2010: Global warming pattern formation: sea surface temperature and rainfall. *J. Climate*, **23**, 966–986.

Yang, X., and coauthors, 2015a: Seasonal predictability of extratropical storm tracks in GFDL's high-resolution climate prediction model. *J. Climate*, **28,** 3592–3611. doi:10.1175/JCLI-D-14-00517.1

Yang, X., and coauthors, 2015b: Extreme North America winter storm season of 2013–14: Roles of radiative forcing, the global warming hiatus and internal variability. [in "Explaining Extremes of 2014 from a Climate Perspective"]. *Bull. Amer. Meteor. Soc.*, S25–S28.

Zhang, L., P. Chang, and L. Ji, 2009: Linking the Pacific Meridional Mode to ENSO: Coupled model analysis. *J. Climate*, **22,** 3488–3505.Zhang, S. and A. Rosati, 2010: An inflated ensemble filter for ocean data assimilation with a biased coupled GCM. *Mon. Wea. Rev.*, **138,** 3905–3931.

Zhang, L., and T. L. Delworth, 2015: Analysis of the characteristics and mechanisms of the Pacific Decadal Oscillaiton in a suite of coupled models from the Geophysical Fluid Dynamics Laboratory. *J. Climate*, **28,** 7678–7701.

Zhang, W., and co-authors, 2016a: Improved Simulation of Tropical Cyclone Responses to ENSO in the Western North Pacific in the High-Resolution GFDL HiFLOR Coupled Climate Model. *J. Climate*, **29,** 1391–1415.

Zhang, W., G. Villarini, G. A. Vecchi, and H. Murakami, 2016b: Statistical-dynamical seasonal forecast of the Western North Pacific and East Asia landfalling tropical cyclones using the high-resolution GFDL FLOR coupled model. *J. Adv. Model. Earth Syst.*, **8,** 538–565.

List of Tables

Table 1 Simulated mean TC frequency during May–November for each basin of the EPO, EEPO, CPO, and the Hawaiian region through the control experiments. Statistical significance

change at 99% significance level is highlighted as asterisk. A bootstrap method is applied for the test.

Table 2 Simulated mean TC frequency by AllForc experiment during May–November for each 20-year period for each basin of the EPO, EEPO, CPO, and the Hawaiian region. Numbers in parentheses indicate changes from the value by the 1941Forc experiment. Statistical significance change at 99% significance level is highlighted as asterisk. A bootstrap method is applied for the test.

List of Figures

FIG. 1 Tropical cyclone (TC) tracks in 2015 and 1997. (a) TC tracks in 2015. Four TCs (red: Guillermo; blue: Hilda; green: Ignacio; purple: Niala) approached the coastal region of Hawaii (red shading). Dots denote TC genesis location. (b) TC tracks in 1997.

FIG. 2 (a) Yearly variability in the observed number of TCs in the EPO during the peak season of May–November, for the period 1966–2015 (gray bars, number) and 2015 (orange bar). Colored lines denote climate indices, in units of standard deviations, for ENSO (Niño-3.4, blue), PMM (red), IPO (purple), PDO (green), and AMO (yellow). For details of the climate indices and methods used to detect them see the Supplementary Information. (b) Yearly variability in the number of TCs in the EEPO (gray) and CPO (yellow), along with the fractional ratio of TC frequency in the CPO relative to EEPO (red line). (c) As in (a), but for frequency of storms approaching the coastal regions of Hawaii. Dashed lines indicate ±σ for TC frequency, whereas solid black line indicates mean value for TC frequency.

FIG. 3 (a, b) Observed sea surface temperature anomaly (SSTA, shading, units=K) during May–November relative to the 1980–2015 mean (contours). (a) SSTA in 2015. (b) SSTA in 1997. (c–f) Idealized SST anomaly prescribed for the sensitivity experiments: (c) observed 2015 SSTA except climatological mean SST in the subtropical central Pacific (SPCLIM), (d) observed 2015 SSTA except climatological mean SST globally outside of the subtropical central Pacific (SPANOM), (e) observed 2015 SSTA except climatological mean SST in the Atlantic Ocean (ATLCLIM), and (f) observed 2015 SSTA except climatological mean SST in the Indian Ocean (INDCLIM). The blue (red) rectangle denotes the subtropical (tropical) region defined in this study.

FIG. 4 Retrospective forecasts of (a) basin-wide TC frequency in the EPO, (b) EEPO, (c) CPO, and (d) TC frequency near Hawaii, during the peak season of May–November initialized from May, for the period 1980–2015 using FLOR. The black line indicates observed TC frequency, green line indicates the mean forecast value, and shading indicates the confidence intervals computed by convolving inter-ensemble spread based on the Poisson distribution. The dots indicate prediction value for each ensemble member. The number for each panel (*cor*) indicates the rank correlation coefficient between the black and green lines.

FIG. 5 Interannual variation of global mean sea surface temperature (SST) simulated by the all forcing (AllForc) multi-decadal experiment from the period 1941–2040. Red thin line shows simulated global mean SST for each ensemble member. Red thick line shows the ensemble mean value. Blue lines are the same as the red lines, but for the experiment with the

constant forcing representative of 1941 conditions (1941Forc). Black arrows denote the major historical volcanic events. The simulated internal variability is out of phase among the ensemble members, whereas the ensemble mean shows a significant positive trend due to the response of anthropogenic forcing along with a few abrupt decreases due to volcanic forcing. For each 20-year period, 700 (20 years × 35 ensemble members) samples are obtained to compute *P(x)*. Reprinted from Murakami et al. (2015a) with modifications.

FIG. 6 Observed anomaly of magnitude of vertical wind shear (contours) superposed on the observed SST anomaly (shadings) and observed locations of TC genesis (blue cross marks) during May–November. Shown are for the seven extremely active TC years of (a) 2015, (c) 1982, (d) 1984, (e) 1985, (f) 1990, (g) 1992, and (h) 2014 in addition to the moderately above normal TC year of (b) 1997 for comparison. The blue and red rectangle domains are defined as the main development regions (MDRs) for TC genesis for the EEPO and CPO, respectively.

FIG. 7 Yearly variability in the observed area mean of large-scale parameters over the CPO and EEPO MDRs. Plotted are (a, b) SST anomaly [SSTA, K]; (c, d) vertical wind shear [VWS, ms^{-1}]; (e, f) relative humidity at 600 hPa [RH600, %]; and (g, h) relative vorticity at 850 hPa [VORT850, $\times 10^{-6}$ s^{-1}]. Left column is for the CPO MDR, whereas right column is for the EEPO MDR. Orange bars highlight the area mean values for 2015. Text in orange denotes the mean value for the 2015 summer season. The number in parenthesis denotes the anomaly for 2015 [units: standard deviation] and the rank based on the 1966–2015 values.

FIG. 8 (a–c) Scatter plots for the observed tropical SST anomaly (10°S–10°N, 170–80°W) versus the subtropical SST anomaly (10–35°N, 150–100°W) during May–November for each year of 1966–2015. The size of circle is proportional to the observed TC genesis frequency for the plotted year. Red circles highlight the years with TC frequency more than one standard deviation. (a) EPO, (b) EEPO, and (c) CPO are shown. (d–f) As in (a–c), but for scatter plots for the observed Niño-3.4 index versus PMM index.

FIG. 9 Composite of anomaly of the large-scale parameters during the year with the subtropical Pacific warming (SUB, left column) and during the years with the tropical Pacific warming (TRP, right column). Contours denote climatological mean value of 1966–2015. Shown are (a, b) SST [K], (c, d) precipitation (only for 1979–2015)[mm day^{-1}], (e, f) Ocean Thermal Energy Potential [10^3 cal cm^{-2}], (g, h) relative humidity at 600 hPa [%], (i, j) vertical wind shear [m s^{-1}], and (k, l) relative vorticity at 850 hPa [10^{-6} s^{-1}]. The blue and red rectangle domains are defined as the main develop regions (MDRs) for TC genesis for the EEPO and CPO, respectively.

FIG. 10 Box plots for predicted 2015 TC frequency, produced by the atmospheric component of FLOR (AM2.5) with various prescribed SST anomaly patterns (see text for details) for (a) EPO, (b) EEPO, (c) CPO, and (d) Hawaiian TCs. The red square shows the ensemble mean, whereas black dot shows each ensemble member. The boxes represent the lower and upper quartiles, the horizontal lines show the median value, and the end lines show the lowest datum still within the 1.5 interquartile range (IQR) of the lower quartile and the highest datum still within the 1.5 IQR of the upper quartile.

FIG. 11 (a) Projected mean SST difference between 1990-control (500-yr) and 1860-control (3500-yr) experiments during May–November [K]. (b) As in (a), but for projected TC genesis density difference [number $\times 10^{-1}$ per 2.5° × 2.5° grid box]. Contour line in (b) indicates that the change is statistical significance at the 99% confidence level or above (bootstrap method). The blue and red rectangle domains are defined as the main develop regions (MDRs) for TC genesis for the EEPO and CPO, respectively.

FIG. 12 Results of *P(x)* from the control simulations for the (a) EPO, (b) EEPO, (c) CPO, and (d) the Hawaiian domain. *P(x)* represents the probability of occurrence of a year with TC number more than or equal to *x*. Red bars are probability obtained from 1860 control simulation (3500 years), whereas blue bars are the results from 1990 control simulation (500 years). Green dots represents FAR computed from Eq. 3.

FIG. 13 Difference in simulated mean SST (K, left column) and TC genesis density (number $\times 10^{-1}$ per 2.5° × 2.5° grid box, right column) between AllForc and 1941Forc experiments for each 20 year period. (a, f) 1941–1960, (b, g) 1961–1980, (c, h) 1981–2000, (d, i) 2001–2020, and (e, j) 2021–2040. The blue and red rectangle domains are defined as the main develop regions (MDRs) for TC genesis for the EEPO and CPO, respectively.

FIG. 14 Probability of equaling or exceeding *x* TC occurrence [*P(x)*] between May and November, from a suite of FLOR simulations. (a) Results of *P(27)* for TC frequency in the EPO, (b) *P(19)* for TC frequency in the EEPO, (c) *P(8)* for TC frequency in the CPO, and (d)

results of *P(4)* for TC frequency near Hawaii, where exceedance thresholds are determined by the extreme 2015 summer season. For each 20-year period, *P(x)* was calculated from 700 samples based on the time-varying all forcing (AllForc) experiment (black line) and fixed anthropogenic forcing at 1941-level (1941Forc) experiment (gray line). Colored bars show the range of conditional *P(x)* induced by natural variability computed by the AllForc experiment for each 20 year period. For example, red bars cover the range of *P(x|PMM+)* and *P(x|PMM–)*, namely, the range of *P(x)* under the conditions between positive PMM and negative PMM phases. Likewise, *P(x)* under the condition of positive and negative phases of PDO (green), ENSO (blue), IPO (purple), and AMO (pink) are shown. Orange circles denote results of *P(x)* from the control simulations. The orange bars show the range of minimum and maximum when *P(x)* is computed for each 100-year period.

FIG. 15 As in Fig. 12, but for the results of the conditional probability of exceedance *P(x|E)* for the period of 2001–2020 from the AllForc multidecadal simulation. Five conditions are considered: E1 is for the years with PMM ≥ +1σ, Niño-3.4 ≥ +1σ, and AMO ≤ –1σ, indicating combined effect of PMM, El Niño, and AMO; E2 is for the years with PMM ≥ +1σ , but Niño-3.4 < +1σ and AMO > –1σ, representing positive PMM only effect; E3 is for the years with Niño-3.4 ≥ +1σ, but PMM < +1σ and AMO > –1σ, representing El Niño only effect; E4 is for the years with AMO ≤ –1σ, but PMM < +1σ and Niño-3.4 < +1σ, indicating AMO only effect; and E5 is for the years with PMM < +1σ, Niño-3.4 < +1σ, and AMO > –1σ, indicating no effect . FAR (circle) is computed from the basis of E5 (i.e., E_0 = E5 in Eq.3), indicating the impact of the single natural variability on the variation of probability of exceedance relative to that without any of PMM, El Niño, and AMO. Sample size for each condition is 25, 104, 96,

57, and 280 for E1, E2, E3, E4, and E5, respectively, from the total sample of 700 (during the 20 years with the 35 ensemble members).

Table 1 Simulated mean TC frequency during May–November for each basin of the EPO, EEPO, CPO, and the Hawaiian region through the control experiments. Statistical significance change at 99% significance level is highlighted as asterisk. A bootstrap method is applied for the test.

Domain	1860-Control	1990-Control	Diff (1990−1860)
EPO	12.0	15.7	+3.7*
EEPO	13.3	15.4	+2.0*
CPO	0.7	1.7	+1.0*
Hawaii	0.2	0.7	+0.5*

* Statistically significant at 99% level

Table 2 Simulated mean TC frequency by AllForc experiment during May–November for each 20-year period for each basin of the EPO, EEPO, CPO, and the Hawaiian region. Numbers in parentheses indicate changes from the value by the 1941Forc experiment. Statistical significance change at 99% significance level is highlighted as asterisk. A bootstrap method is applied for the test.

Domain	1941−1960	1961−1980	1981−2000	2001−2020	2021−2040
EPO	15.8 (+0.2)	16.7 (+1.6*)	16.7 (+1.9*)	16.9 (+1.3*)	17.1 (+1.4*)
EEPO	15.1 (+0.3)	15.6 (+1.3*)	15.6 (+1.4*)	15.2 (+0.4)	15.2 (+0.4)
CPO	1.4 (−0.1)	1.7 (+0.4*)	1.7 (+0.4*)	2.0 (+0.5*)	2.3 (+0.8*)
Hawaii	0.5 (−0.1)	0.7 (+0.3*)	0.7 (+0.3*)	1.0 (+0.5*)	1.1 (+0.6*)

* Statistically significant at 99% level

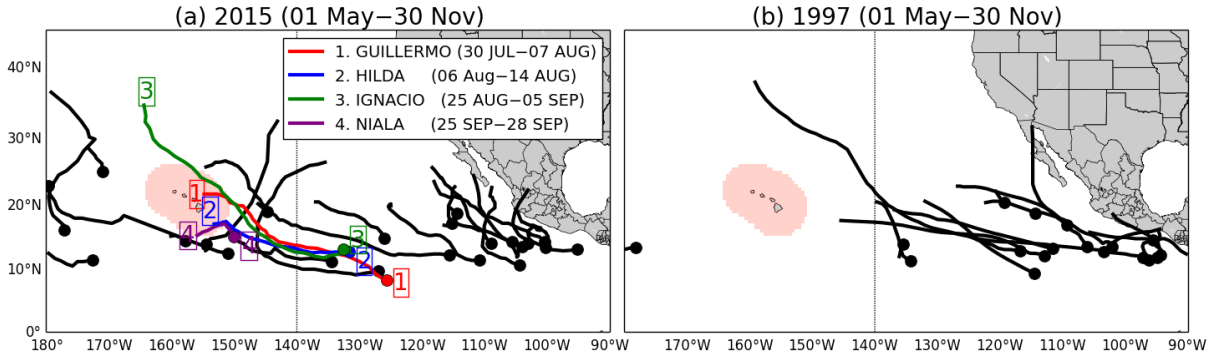

FIG. 1 Tropical cyclone (TC) tracks in 2015 and 1997. (a) TC tracks in 2015. Four TCs (red: Guillermo; blue: Hilda; green: Ignacio; purple: Niala) approached the coastal region of Hawaii (red shading). Dots denote TC genesis location. (b) TC tracks in 1997.

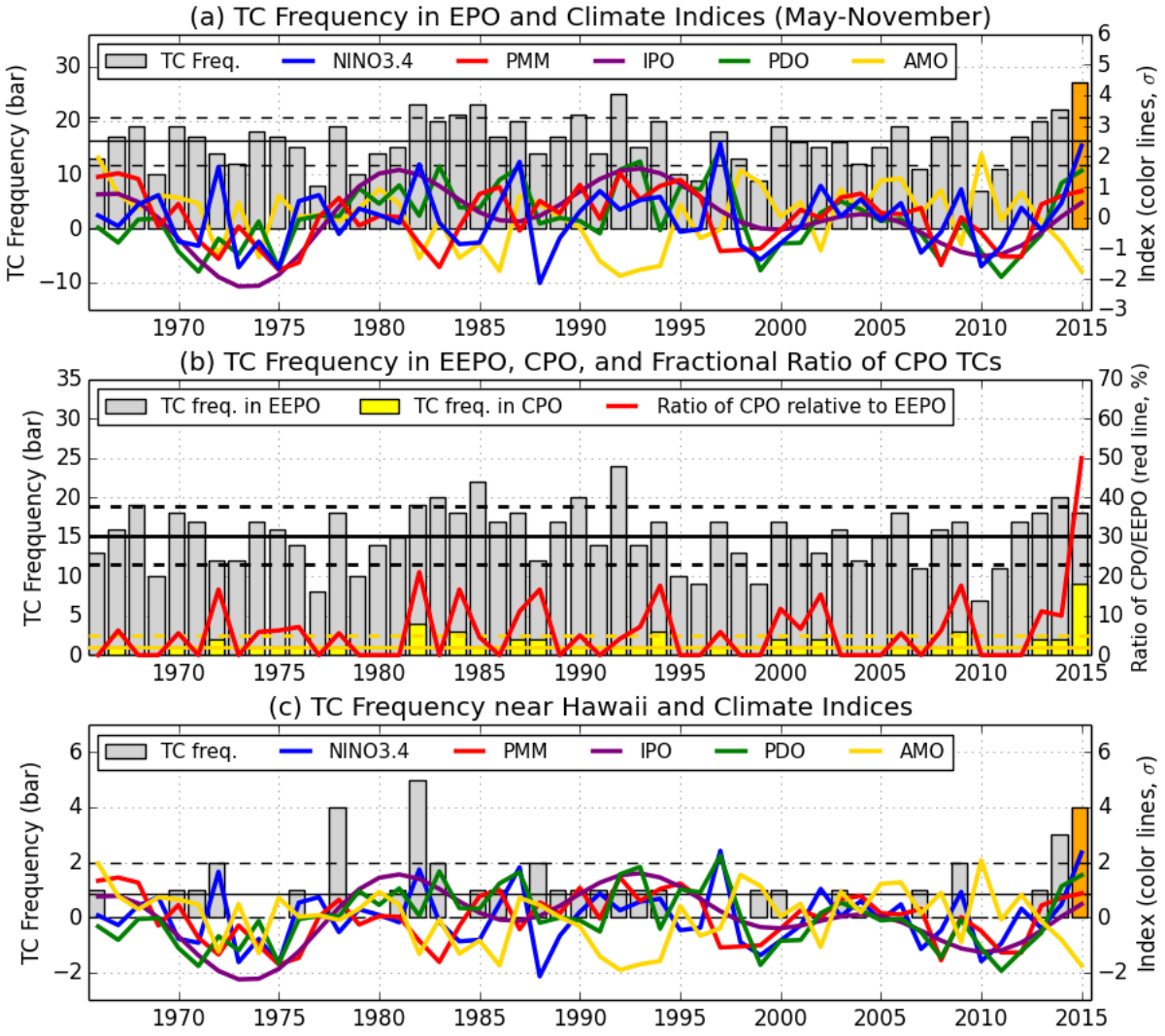

FIG. 2 (a) Yearly variability in the observed number of TCs in the EPO during the peak season of May–November, for the period 1966–2015 (gray bars, number) and 2015 (orange bar). Colored lines denote climate indices, in units of standard deviations, for ENSO (Niño-3.4, blue), PMM (red), IPO (purple), PDO (green), and AMO (yellow). For details of the climate indices and methods used to detect them see the Supplementary Information. (b) Yearly variability in the number of TCs in the EEPO (gray) and CPO (yellow), along with the fractional ratio of TC frequency in the CPO relative to EEPO (red line). (c) As in (a), but for frequency of storms approaching the coastal regions of Hawaii. Dashed lines indicate ±σ for TC frequency, whereas solid black line indicates mean value for TC frequency.

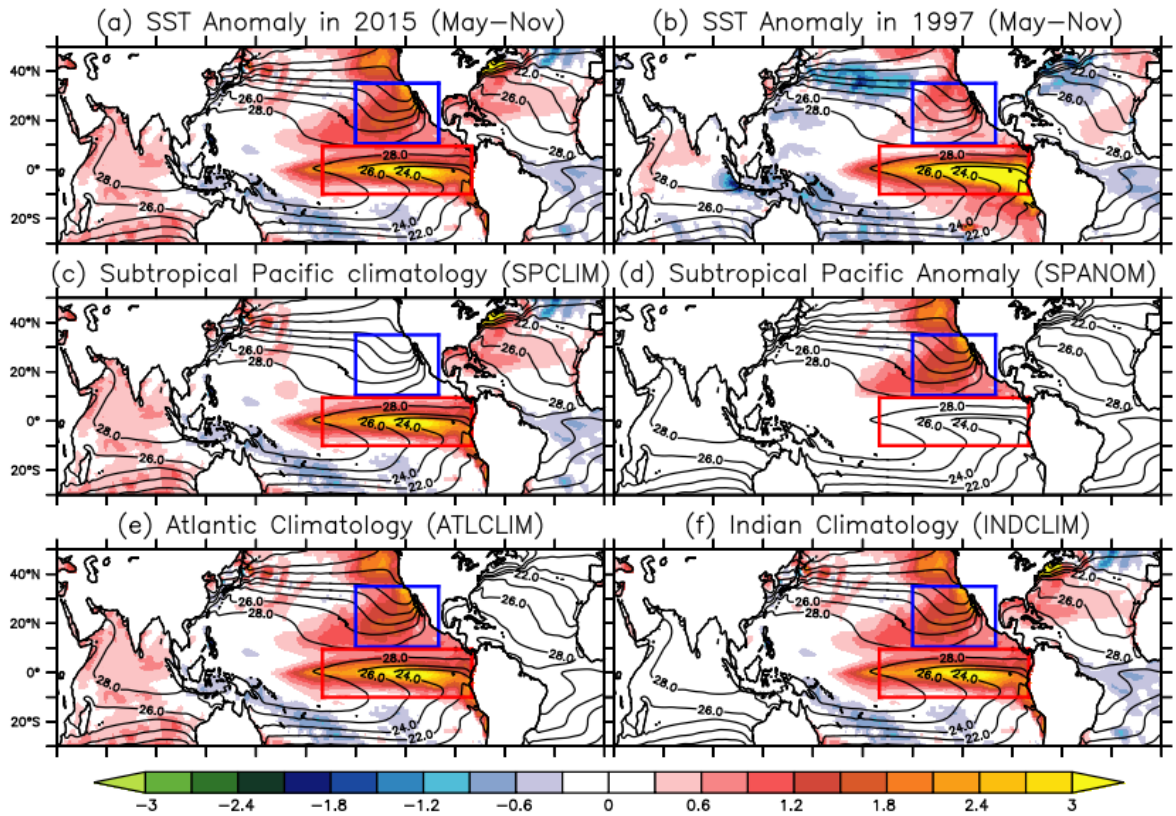

FIG. 3 (a, b) Observed sea surface temperature anomaly (SSTA, shading, units=K) during May–November relative to the 1980–2015 mean (contours). (a) SSTA in 2015. (b) SSTA in 1997. (c–f) Idealized SST anomaly prescribed for the sensitivity experiments: (c) observed 2015 SSTA except climatological mean SST in the subtropical central Pacific (SPCLIM), (d) observed 2015 SSTA except climatological mean SST globally outside of the subtropical central Pacific (SPANOM), (e) observed 2015 SSTA except climatological mean SST in the Atlantic Ocean (ATLCLIM), and (f) observed 2015 SSTA except climatological mean SST in the Indian Ocean (INDCLIM). The blue (red) rectangle denotes the subtropical (tropical) region defined in this study.

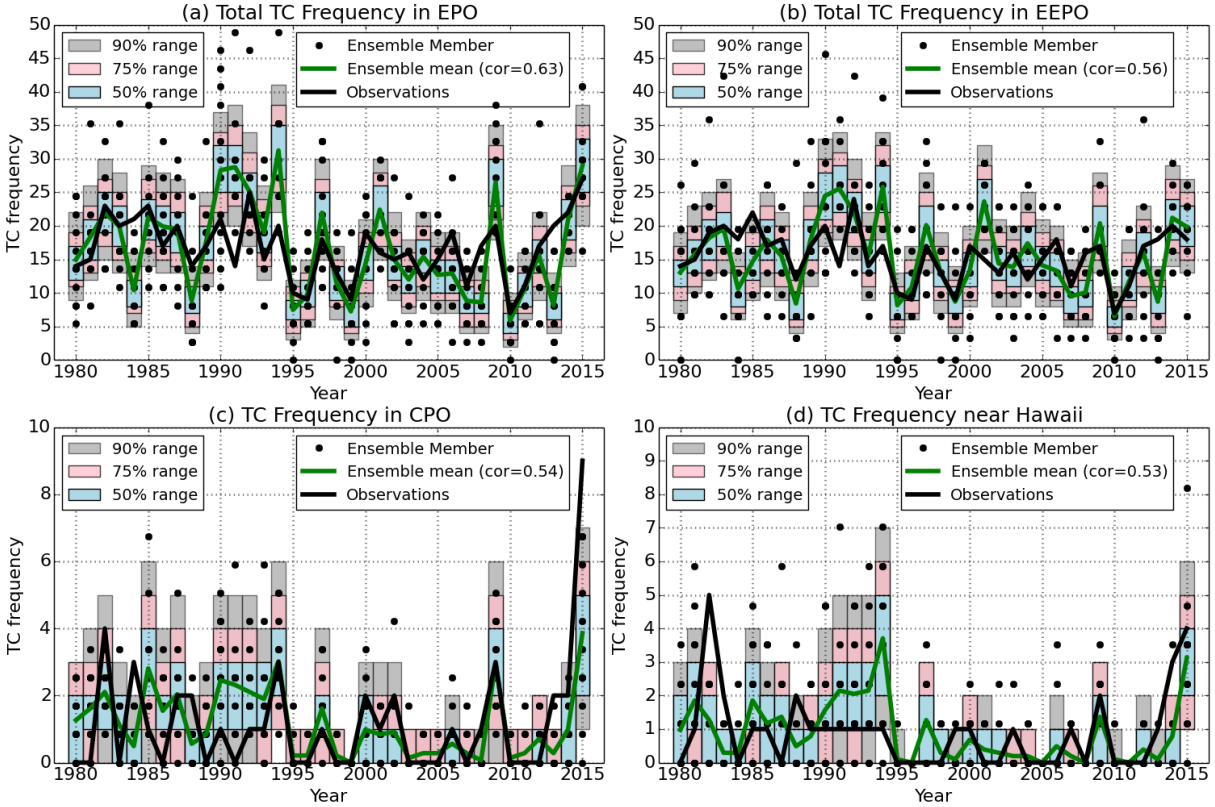

FIG. 4 Retrospective forecasts of (a) basin-wide TC frequency in the EPO, (b) EEPO, (c) CPO, and (d) TC frequency near Hawaii, during the peak season of May–November initialized from May, for the period 1980–2015 using FLOR. The black line indicates observed TC frequency, green line indicates the mean forecast value, and shading indicates the confidence intervals computed by convolving inter-ensemble spread based on the Poisson distribution. The dots indicate prediction value for each ensemble member. The number for each panel (*cor*) indicates the rank correlation coefficient between the black and green lines.

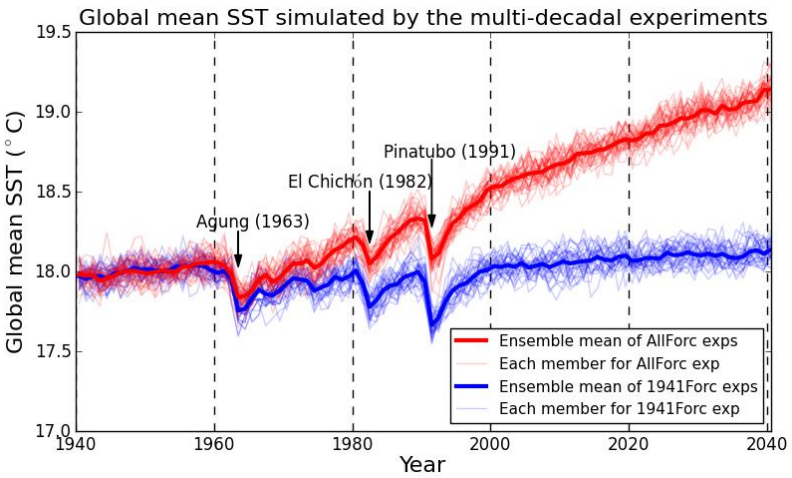

FIG. 5 Interannual variation of global mean sea surface temperature (SST) simulated by the all forcing (AllForc) multi-decadal experiment from the period 1941–2040. Red thin line shows simulated global mean SST for each ensemble member. Red thick line shows the ensemble mean value. Blue lines are the same as the red lines, but for the experiment with the constant forcing representative of 1941 conditions (1941Forc). Black arrows denote the major historical volcanic events. The simulated internal variability is out of phase among the ensemble members, whereas the ensemble mean shows a significant positive trend due to the response of anthropogenic forcing along with a few abrupt decreases due to volcanic forcing. For each 20-year period, 700 (20 years × 35 ensemble members) samples are obtained to compute *P(x)*. Reprinted from Murakami et al. (2015a) with modifications.

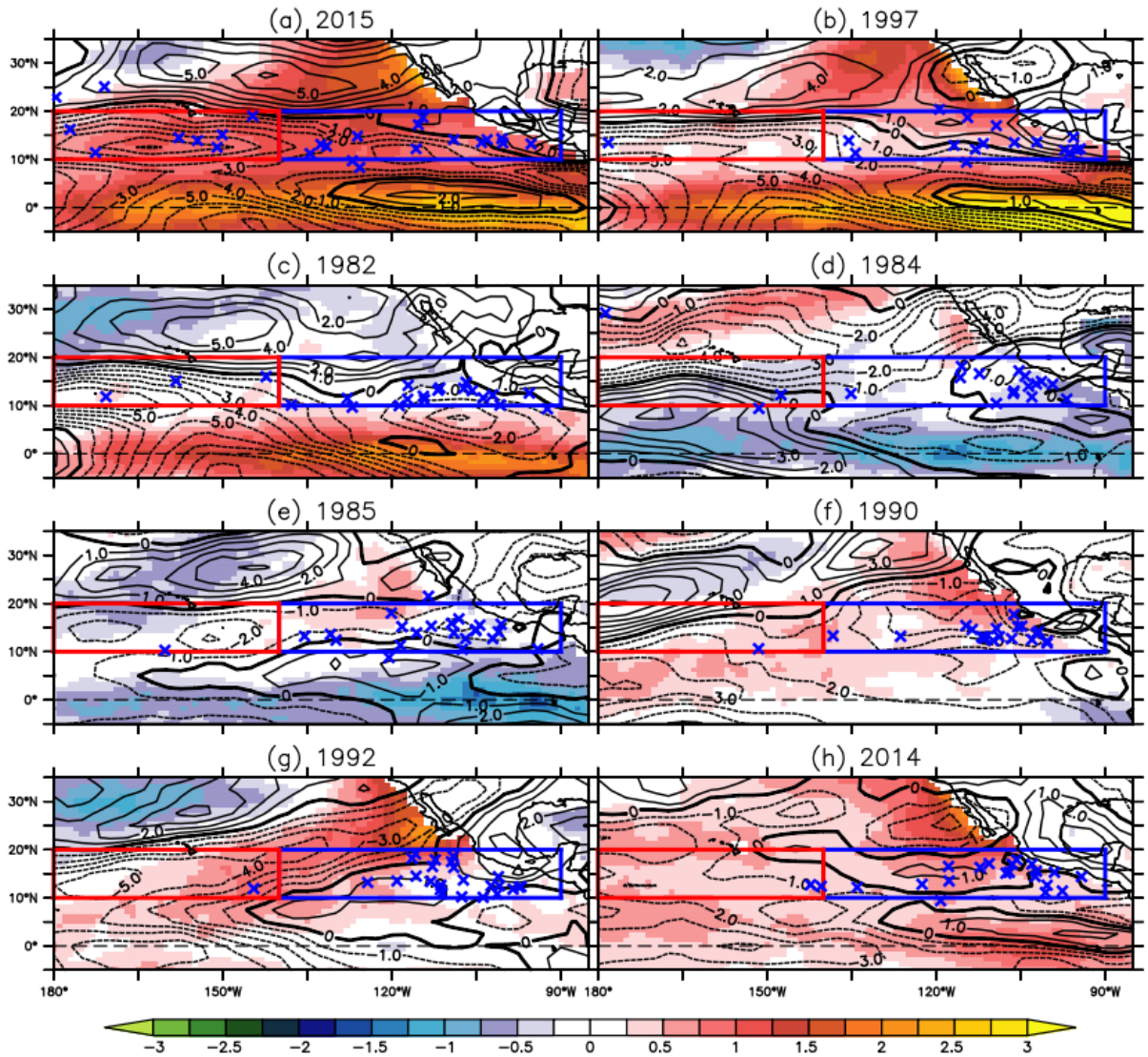

FIG. 6 Observed anomaly of magnitude of vertical wind shear (contours) superposed on the observed SST anomaly (shadings) and observed locations of TC genesis (blue cross marks) during May–November. Shown are for the seven extremely active TC years of (a) 2015, (c) 1982, (d) 1984, (e) 1985, (f) 1990, (g) 1992, and (h) 2014 in addition to the moderately above normal TC year of (b) 1997 for comparison. The blue and red rectangle domains are defined as the main develop regions (MDRs) for TC genesis for the EEPO and CPO, respectively.

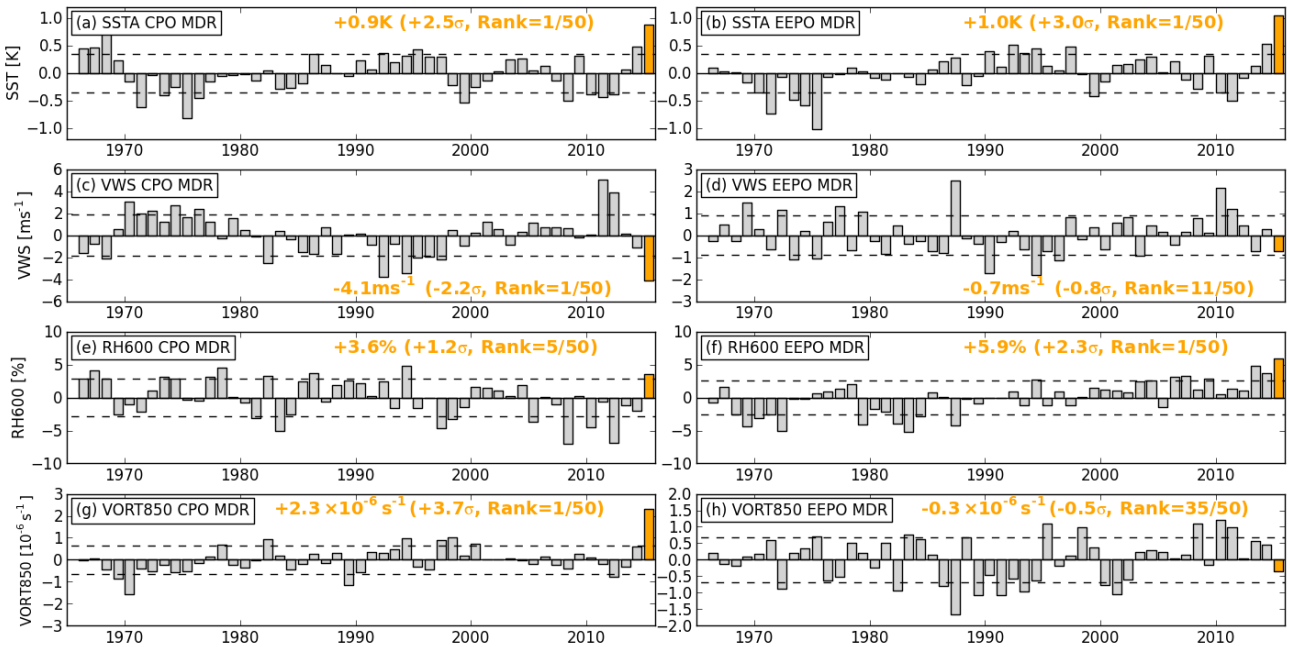

FIG. 7 Yearly variability in the observed area mean of large-scale parameters over the CPO and EEPO MDRs. Plotted are (a, b) SST anomaly [SSTA, K]; (c, d) vertical wind shear [VWS, ms^{-1}]; (e, f) relative humidity at 600 hPa [RH600, %]; and (g, h) relative vorticity at 850 hPa [VORT850, $\times 10^{-6}$ s^{-1}]. Left column is for the CPO MDR, whereas right column is for the EEPO MDR. Orange bars highlight the area mean values for 2015. Text in orange denotes the mean value for the 2015 summer season. The number in parenthesis denotes the anomaly for 2015 [units: standard deviation] and the rank based on the 1966–2015 values.

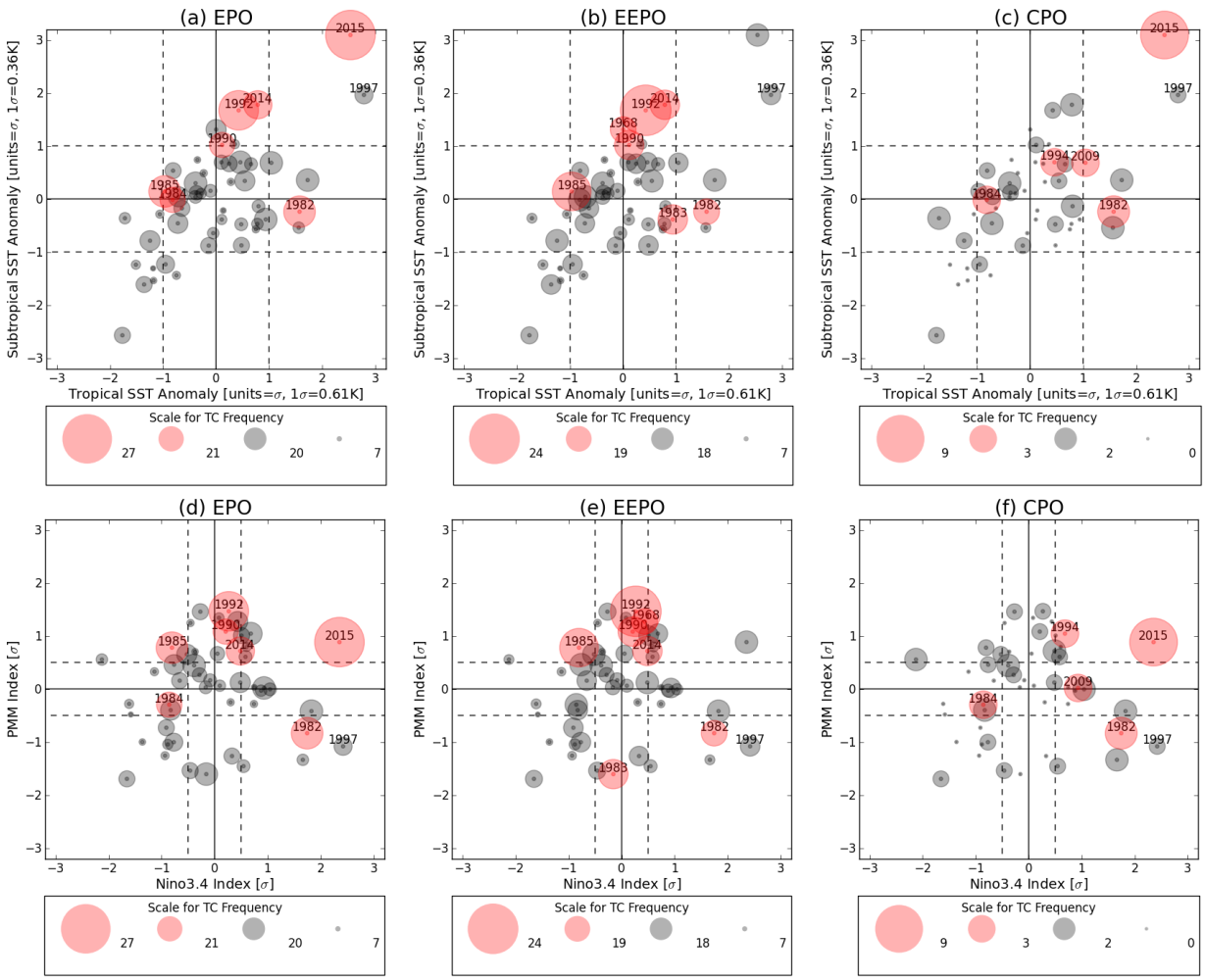

FIG. 8 (a–c) Scatter plots for the observed tropical SST anomaly (10°S–10°N, 170–80°W) versus the subtropical SST anomaly (10–35°N, 150–100°W) during May–November for each year of 1966–2015. The size of circle is proportional to the observed TC genesis frequency for the plotted year. Red circles highlight the years with TC frequency more than one standard deviation. (a) EPO, (b) EEPO, and (c) CPO are shown. (d–f) As in (a–c), but for scatter plots for the observed Niño-3.4 index versus PMM index.

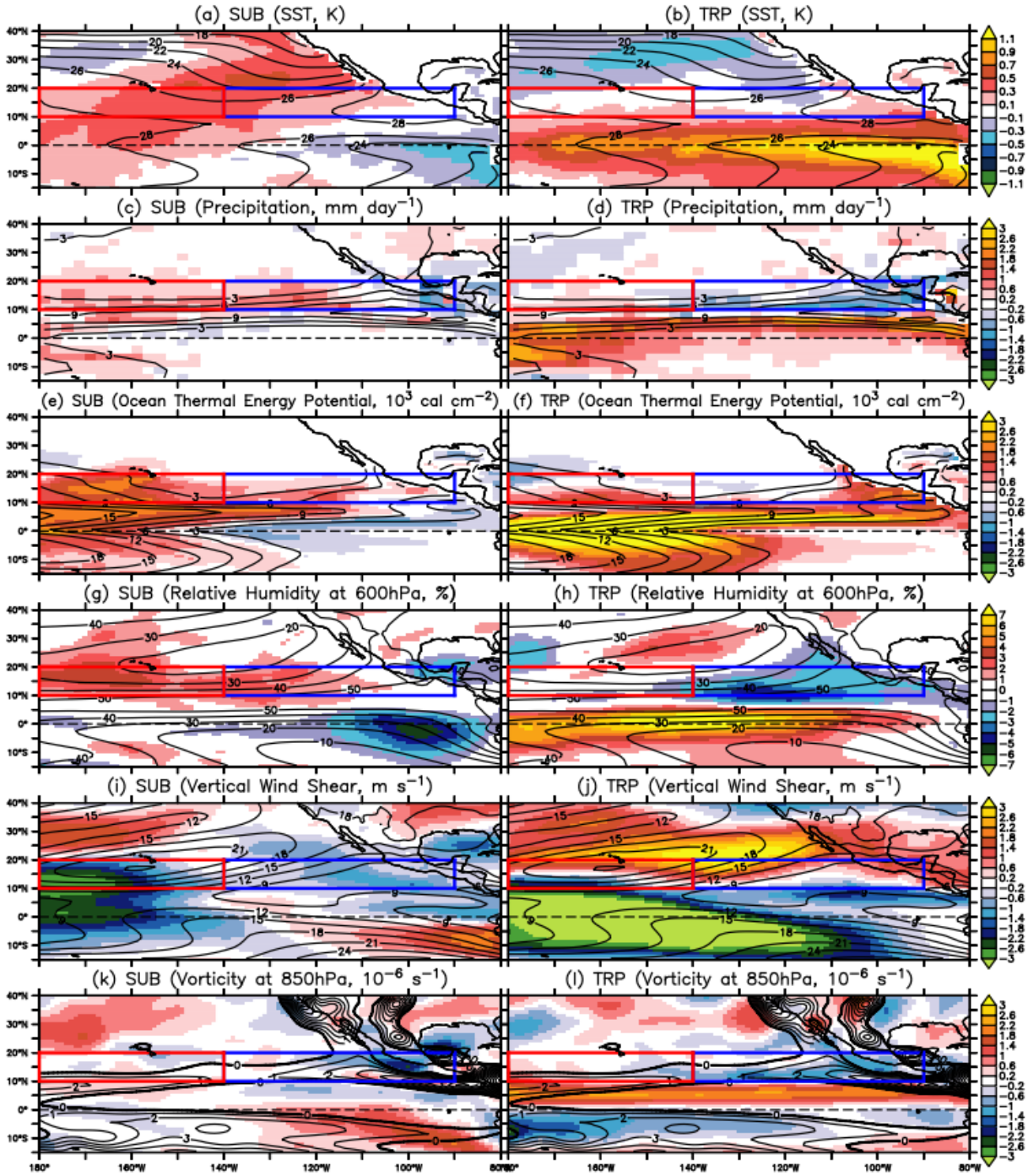

FIG. 9 Composite of anomaly of the large-scale parameters during the year with the subtropical Pacific warming (SUB, left column) and during the years with the tropical Pacific warming (TRP, right column). Contours denote climatological mean value of 1966–2015. Shown are (a, b) SST [K], (c, d) precipitation (only for 1979–2015)[mm day^{-1}], (e, f) Ocean Thermal Energy Potential [10^3 cal cm^{-2}], (g, h) relative humidity at 600 hPa [%], (i, j) vertical wind shear [m s^{-1}], and (k, l) relative vorticity at 850 hPa [10^{-6} s^{-1}]. The blue and red rectangle domains are defined as the main develop regions (MDRs) for TC genesis for the EEPO and CPO, respectively.

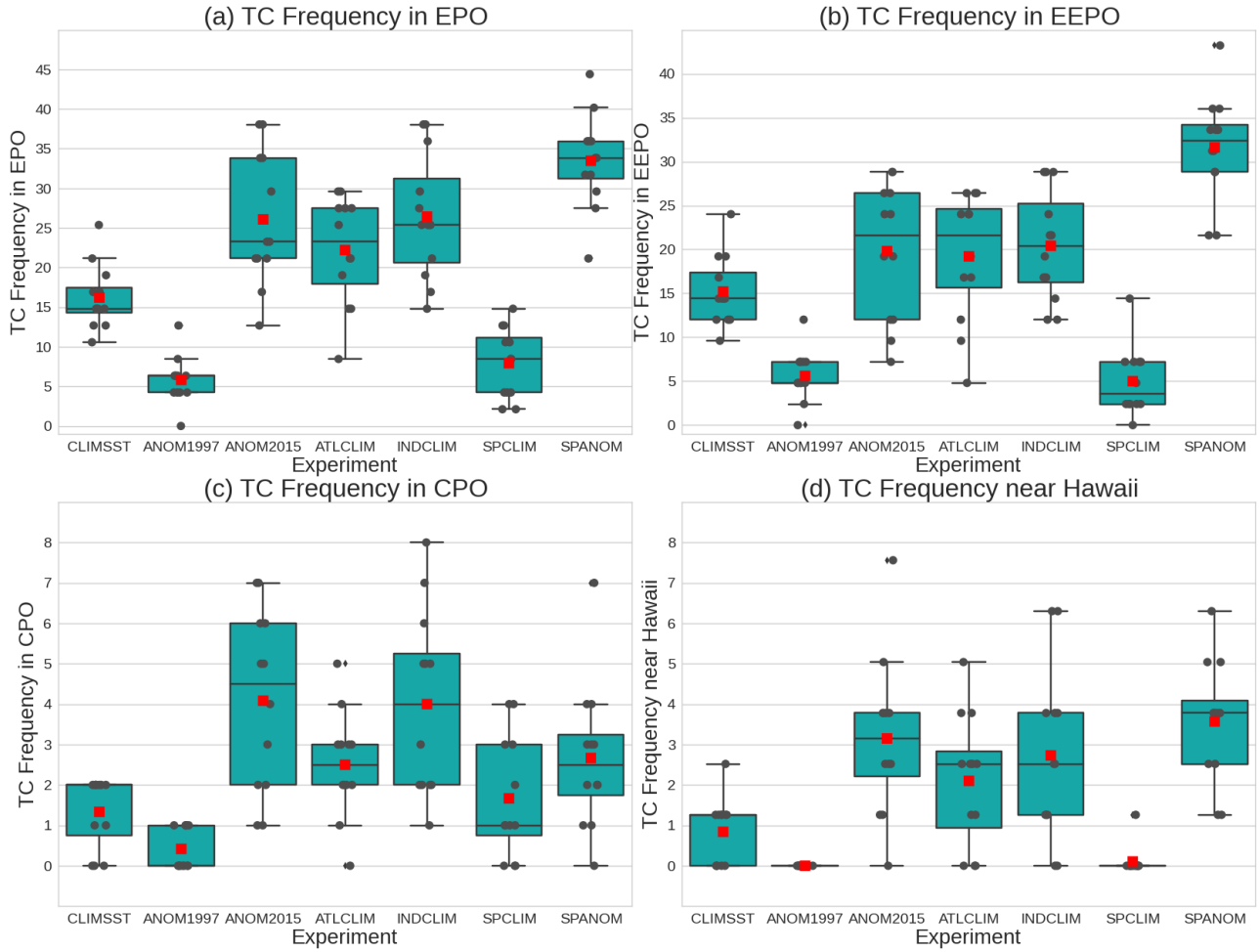

FIG. 10 Box plots for predicted 2015 TC frequency, produced by the atmospheric component of FLOR (AM2.5) with various prescribed SST anomaly patterns (see text for details) for (a) EPO, (b) EEPO, (c) CPO, and (d) Hawaiian TCs. The red square shows the ensemble mean, whereas black dot shows each ensemble member. The boxes represent the lower and upper quartiles, the horizontal lines show the median value, and the end lines show the lowest datum still within the 1.5 interquartile range (IQR) of the lower quartile and the highest datum still within the 1.5 IQR of the upper quartile.

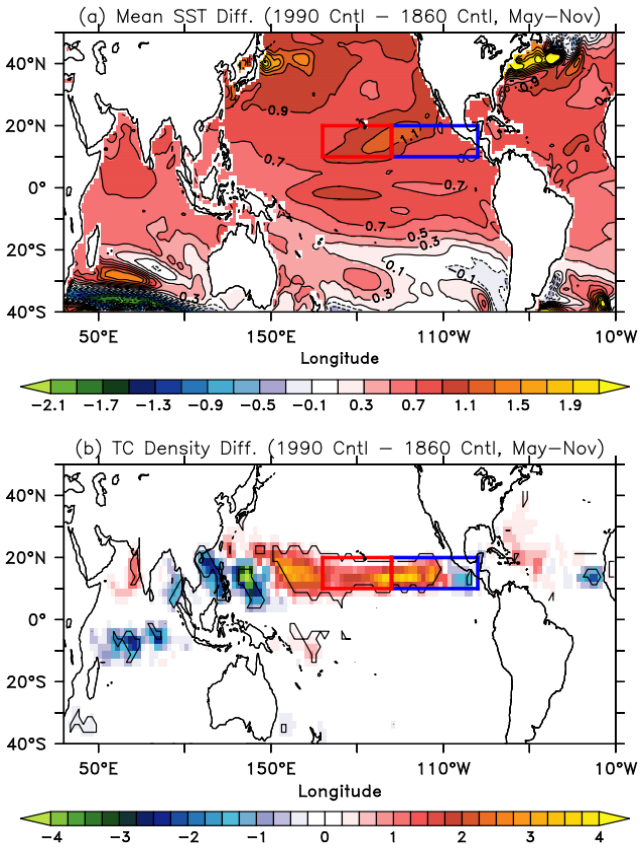

FIG. 11 (a) Projected mean SST difference between 1990-control (500-yr) and 1860-control (3500-yr) experiments during May–November [K]. (b) As in (a), but for projected TC genesis density difference [number $\times 10^{-1}$ per 2.5° × 2.5° grid box]. Contour line in (b) indicates that the change is statistical significance at the 99% confidence level or above (bootstrap method). The blue and red rectangle domains are defined as the main develop regions (MDRs) for TC genesis for the EEPO and CPO, respectively.

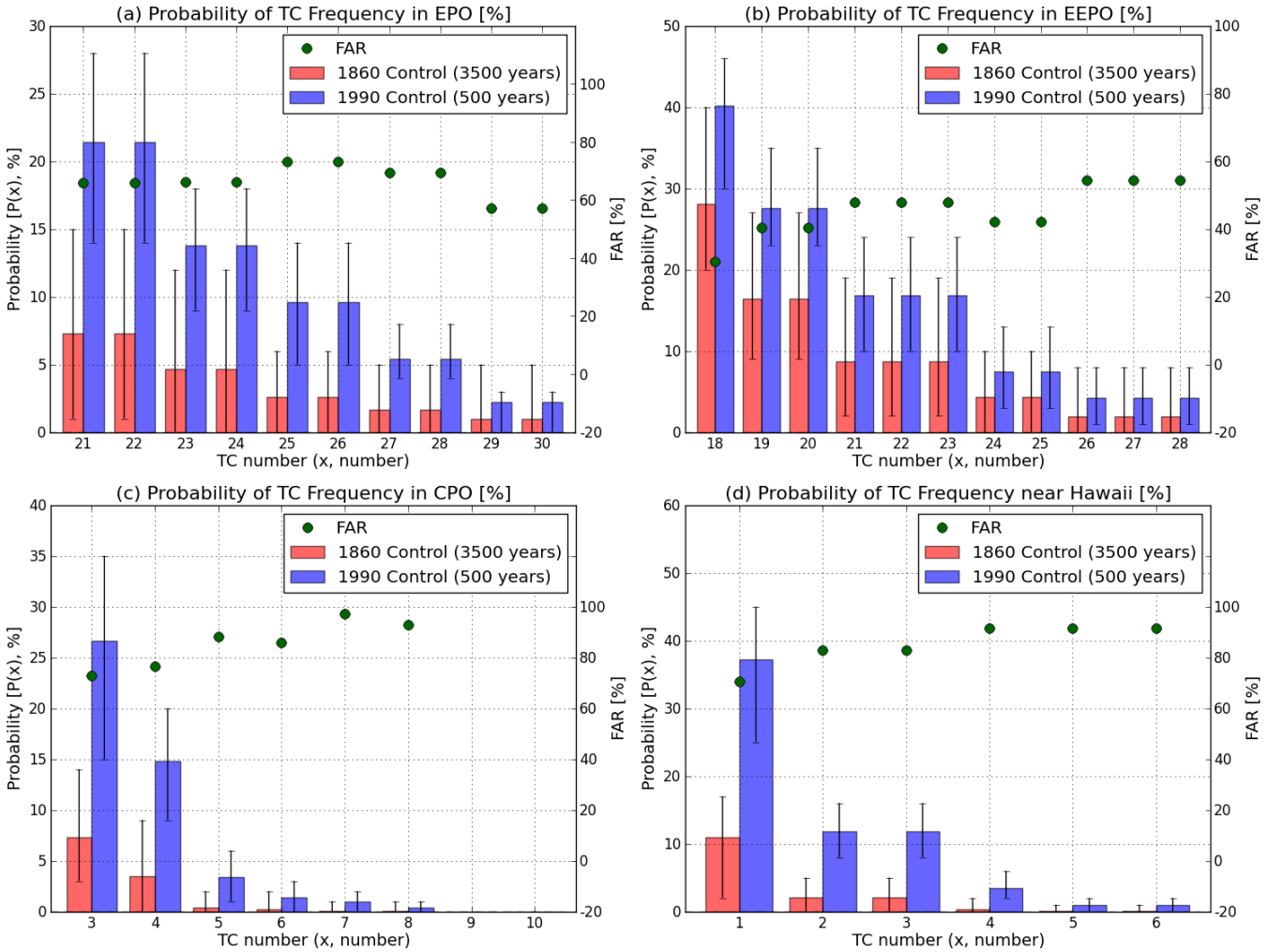

FIG. 12 Results of *P(x)* from the control simulations for the (a) EPO, (b) EEPO, (c) CPO, and (d) the Hawaiian domain. *P(x)* represents the probability of occurrence of a year with TC number more than or equal to *x*. Red bars are probability obtained from 1860 control simulation (3500 years), whereas blue bars are the results from 1990 control simulation (500 years). Green dots represents FAR computed from Eq. 3.

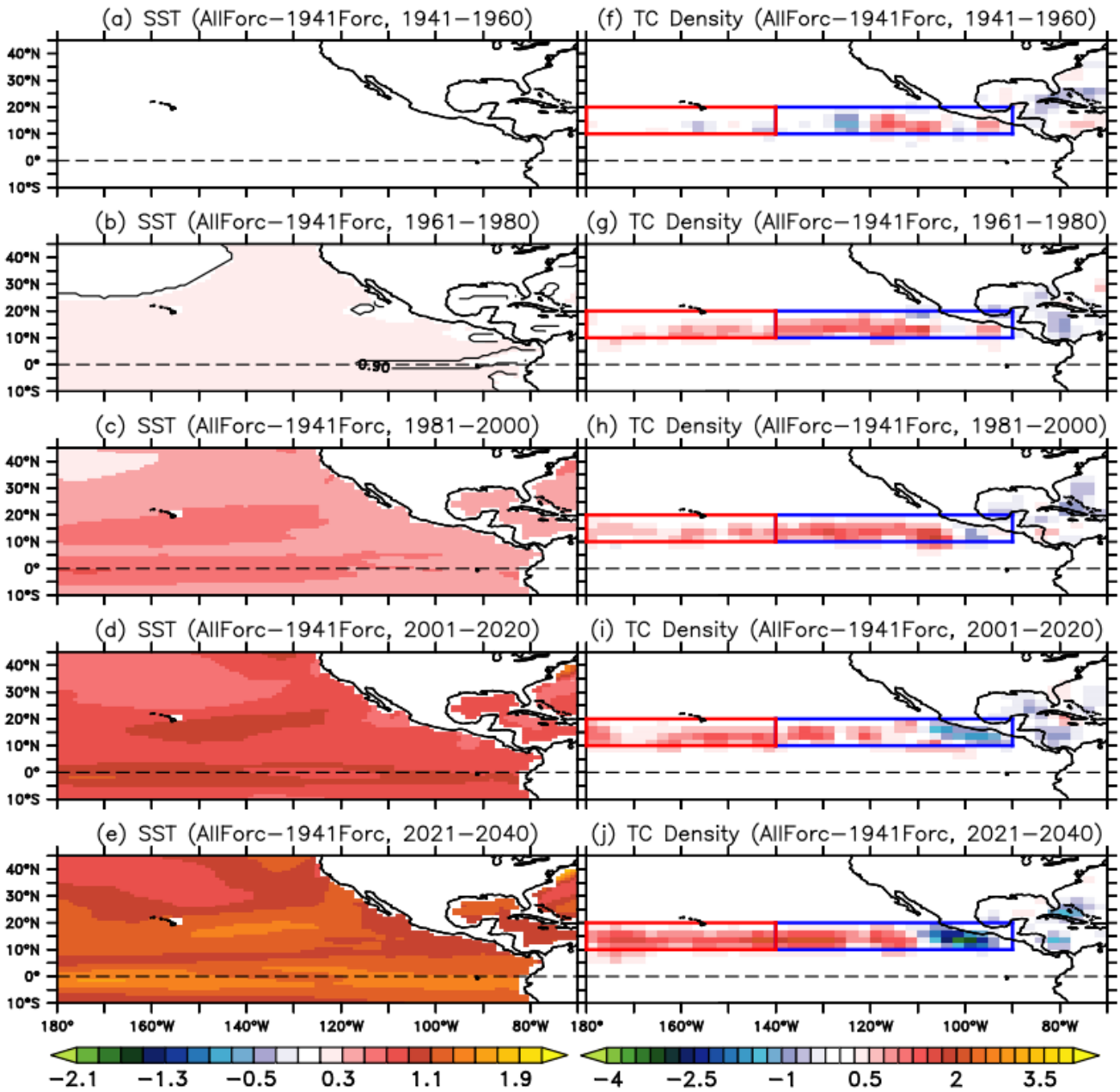

FIG. 13 Difference in simulated mean SST (K, left column) and TC genesis density (number $\times 10^{-1}$ per 2.5° × 2.5° grid box, right column) between AllForc and 1941Forc experiments for each 20 year period. (a, f) 1941–1960, (b, g) 1961–1980, (c, h) 1981–2000, (d, i) 2001–2020, and (e, j) 2021–2040. The blue and red rectangle domains are defined as the main develop regions (MDRs) for TC genesis for the EEPO and CPO, respectively.

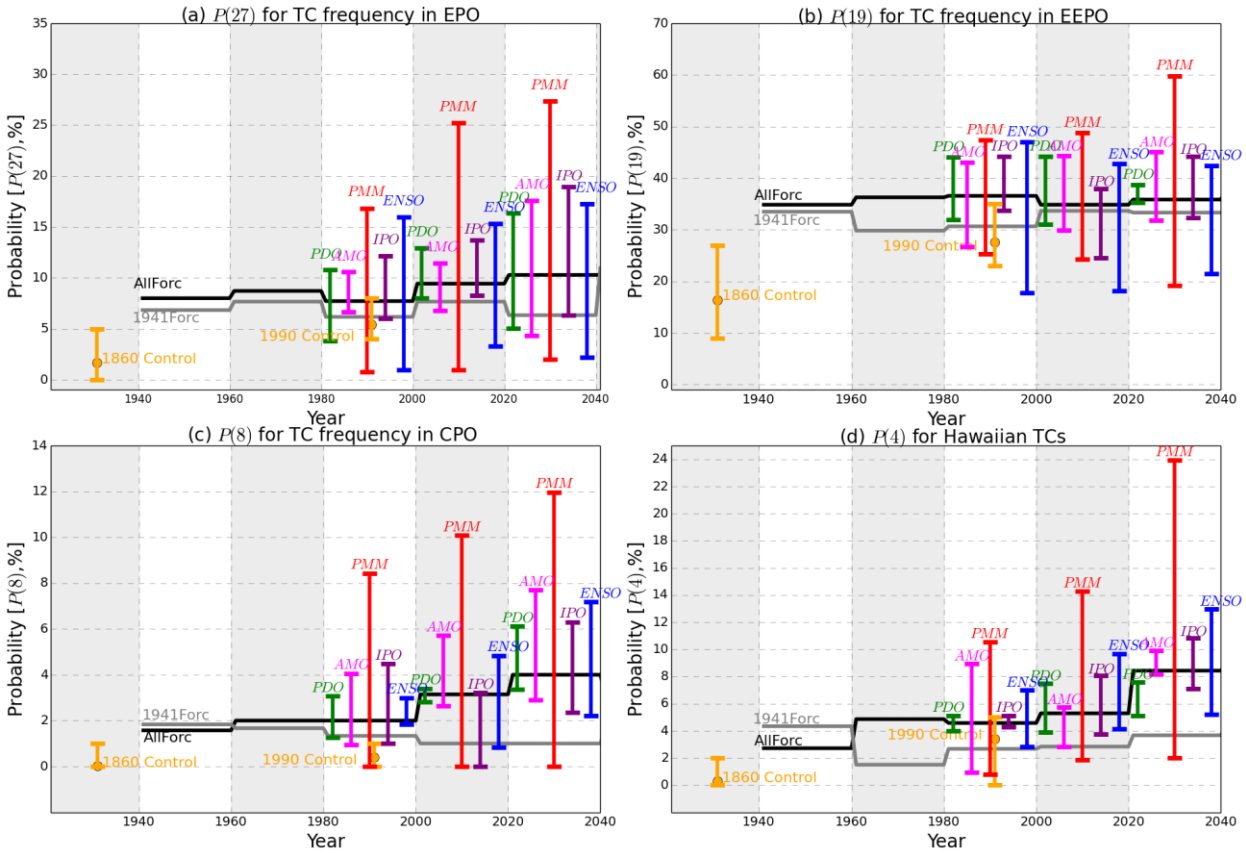

FIG. 14 Probability of equaling or exceeding *x* TC occurrence [*P(x)*] between May and November, from a suite of FLOR simulations. (a) Results of *P(27)* for TC frequency in the EPO, (b) *P(19)* for TC frequency in the EEPO, (c) *P(8)* for TC frequency in the CPO, and (d) results of *P(4)* for TC frequency near Hawaii, where exceedance thresholds are determined by the extreme 2015 summer season. For each 20-year period, *P(x)* was calculated from 700 samples based on the time-varying all forcing (AllForc) experiment (black line) and fixed anthropogenic forcing at 1941-level (1941Forc) experiment (gray line). Colored bars show the range of conditional *P(x)* induced by natural variability computed by the AllForc experiment for each 20 year period. For example, red bars cover the range of *P(x|PMM+)* and *P(x|PMM–)*, namely, the range of *P(x)* under the conditions between positive PMM and negative PMM phases. Likewise, *P(x)* under the condition of positive and negative phases of PDO (green), ENSO (blue), IPO (purple), and AMO (pink) are shown. Orange circles denote results of *P(x)* from the control simulations. The orange bars show the range of minimum and maximum when *P(x)* is computed for each 100-year period.

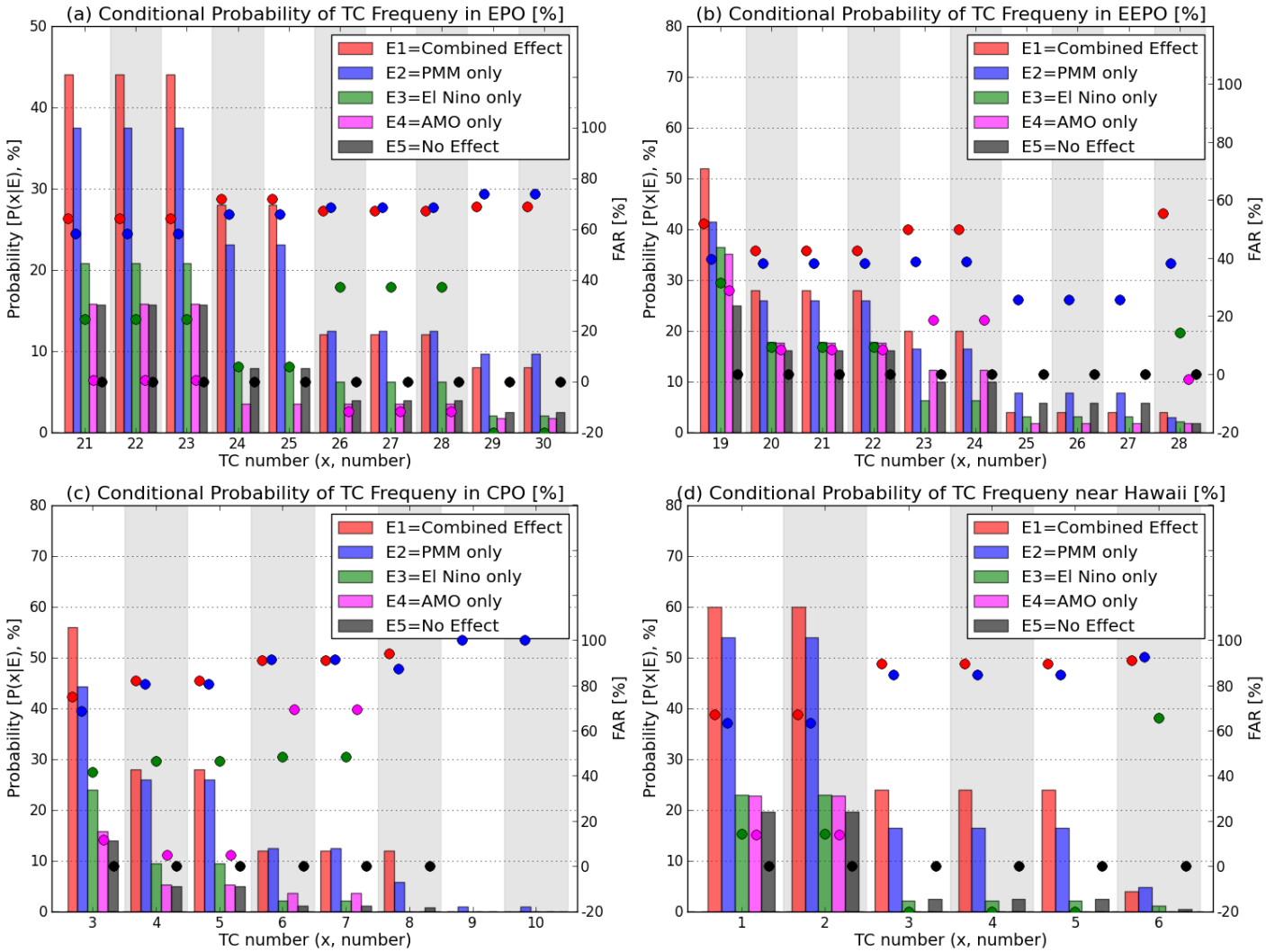

FIG. 15 As in Fig. 12, but for the results of the conditional probability of exceedance *P(x|E)* for the period of 2001–2020 from the AllForc multidecadal simulation. Five conditions are considered: E1 is for the years with PMM ≥ +1σ, Niño-3.4 ≥ +1σ, and AMO ≤ –1σ, indicating combined effect of PMM, El Niño, and AMO; E2 is for the years with PMM ≥ +1σ , but Niño-3.4 < +1σ and AMO > –1σ, representing positive PMM only effect; E3 is for the years with Niño-3.4 ≥ +1σ, but PMM < +1σ and AMO > –1σ, representing El Niño only effect; E4 is for the years with AMO ≤ –1σ, but PMM < +1σ and Niño-3.4 < +1σ, indicating AMO only effect; and E5 is for the years with PMM < +1σ, Niño-3.4 < +1σ, and AMO > –1σ, indicating no effect . FAR (circle) is computed from the basis of E5 (i.e., E_0 = E5 in Eq.3), indicating the impact of the single natural variability on the variation of the probability of exceedance relative to that without any of PMM, El Niño, and AMO. Sample size for each condition is 25, 104, 96, 57, and 280 for E1, E2, E3, E4, and E5, respectively, from the total sample of 700 (during the 20 years with the 35 ensemble members).